Composite Duty Modulation of Dual Active Bridge Converters to Minimize Output Voltage Ripples and Inductor RMS Currents

Xiaofeng Wang, *Student Member, IEEE*, Ming Yang, *Senior Member, IEEE*, Wenxia Sima, *Member, IEEE*, Tao Yuan, *Member, IEEE*, Potao Sun, *Member, IEEE*, and Shuoyan Lin

***Abstract*—To reduce output voltage ripples and inductor rms currents, a composite duty modulation (CDM) scheme of dual active bridge (DAB) converters is proposed, which can overcome the limits of fundamental duty modulation under light load and multi-order reactive-current suppression strategy under heavy load. The output voltage ripple and inductor current of the DAB converter are represented by a generalized averaging model considering the second harmonic component. The proposed CDM scheme can be implemented easily by modulating the duty ratio of the ac voltage not requiring a complex modeling process, offline calculation, and additional current sensor. The improved CDM scheme has also been proposed to optimize CDM performance when the voltage conversion ratio approaches unity under light load. The output voltage ripple optimization, inductor rms current suppression, and efficiency improvement of the proposed method are validated by simulation and experimental comparisons with other modulation schemes under different voltage conversion ratios and load conditions.**

***Index Terms*—Dual active bridge (DAB) converter, minimum current operation, modulation scheme, voltage ripple.**

I. INTRODUCTION

DUAL active bridge (DAB) converters are prevalent in dc microgrids and distributed power supply systems because of high power density, adjustable voltage conversion ratio, soft-switching, galvanic isolation, and bidirectional power transmission [1], [2], [3], which can also be applied to power conversion for high-speed railway, electric vehicle, more-electric aircraft, and renewable power regeneration [4], [5], [6], [7], [8].

Various modulation schemes have been proposed to improve the performance of DAB converters in recent years [9]. The classic phase-shift (PS) modulation schemes of DAB converters can be classified into four categories according to control variables [10], [11], [12], namely, single-PS (SPS) modulation, extended-PS (EPS) modulation, dual-PS (DPS) modulation, and triple-PS (TPS) modulation [13], [14]. Given that TPS modulation has three control variables, many optimal modulation strategies are based on it because of more flexible freedom and better performance [15]. The analysis methods of various modulation schemes of DAB can be categorized into frequency-domain analysis (FDA) and time-domain analysis (TDA) [16]. TDA is accurate and widely used in different modulation schemes. However, huge online or offline computations are required when using TDA [16]. FDA can be applied to the whole operation range without working mode classification and can extend to three-phase DAB easily [16], [17], [18]. Hence, FDA is selected to analyze DAB converters in many modulation schemes [16], [17], [18], [19], [20], [21].

Different optimization objects are adopted in modulation strategies for the enhancement of performance and efficiency of DAB converters, such as inductor peak current [22], inductor rms current [15], power loss [23], [24], reactive power or backflow power [20]. Nowadays, most studies focus on the optimization of inductor peak current or rms current for efficiency improvement and electrical stress reduction, considering feasibility and effectiveness [25], [26], [27], [28], [29], [30], [31].

From the perspective of inductor peak current $I_{L\mathrm{pk}}$, a unified PS (UPS) modulation method, adopting TDA, is proposed in [25] on the basis of the Lagrange multiplier method to acquire the optimal solution. However, UPS cannot obtain the global optimum [26]. The deep reinforcement learning (DRL)-aided modulation scheme does not need accurate model information and can provide efficient solutions for the optimization problem of DAB converters [27]. However, the algorithm is weak to hyperparameter, and a large generated lookup table is needed [19], [20]. Asymmetrical duty modulation (ADM) is proposed to optimize the peak current and widen the zero voltage switching (ZVS) region of DAB converters [21], [28]. Nevertheless, the current stress under ADM is higher than other TPS schemes at medium load [29]. Although an optimal primary-side duty modulation (OPDM) can alleviate the ADM current stress, OPDM performance can be improved when the load is light [29]. A five-degree-of-freedom modulation scheme can be used to further optimize the characteristics of DAB converters [22]. However, implementing online calculations is complicated [29].

Inductor rms current $I_{L\mathrm{rms}}$ can represent the conduction loss more accurately than the peak current [30]. The inductor rms

Manuscript received 23 October 2023; revised 3 January 2024; accepted 21 January 2024. Date of publication 24 January 2024; date of current version 20 March 2024. This work was supported in part by the National Natural Science Foundation of China under Grants 52377136 and 51977018. Recommended for publication by Associate Editor Y. Siwakoti. *(Corresponding authors: Ming Yang; Wenxia Sima.)*

The authors are with the State Key Laboratory of Power Transmission Equipment and System Security and New Technology, Chongqing University, Chongqing 400044, China (e-mail: xiaofengwang@cqu.edu.cn; cqucee@cqu.edu.cn; cqsmwx@cqu.edu.cn; yuantao_cq@cqu.edu.cn; sunpotao@cqu.edu.cn; linshuoyan@cqu.edu.cn).

Color versions of one or more figures in this article are available at https://doi.org/10.1109/TPEL.2024.3358023.

Digital Object Identifier 10.1109/TPEL.2024.3358023

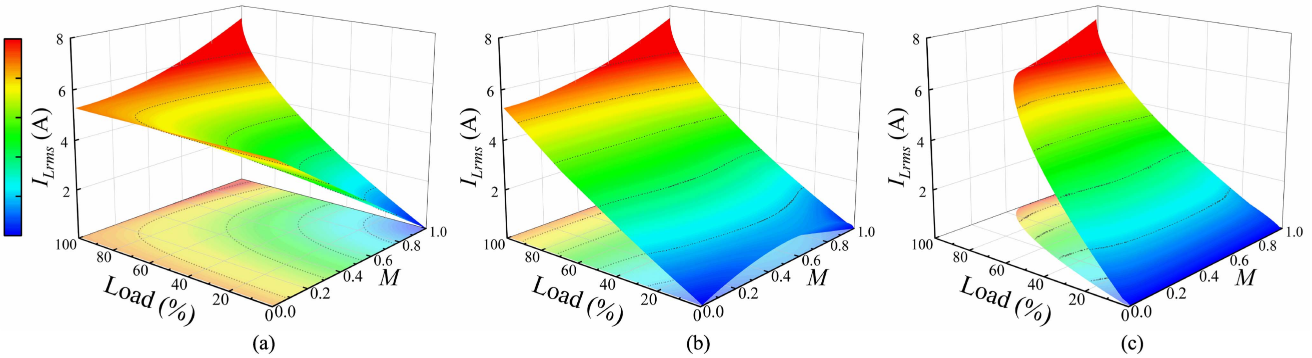

Fig. 1. Inductor rms current I_{Lrms} of a DAB converter (see Fig. 2) calculated with circuit parameters in Table I at various load conditions and voltage conversion ratio M. (a) SPS. (b) FDM. (c) MRS.

current of SPS modulation is shown in Fig. 1(a). SPS modulation is the simplest scheme with only one control variable. However, it has poor steady-state characteristics at light load and nonunity voltage conversion ratio. Global optimal condition (GOC) equations are proposed to minimize rms currents and realize efficiency improvement [26]. However, the complex analysis and equation solving of different modes are needed in GOC. Meanwhile, the offline particle swarm optimization (PSO) algorithm is used to calculate a set of optical control variables for rms current minimization [31]. Nevertheless, PSO is difficult to realize online calculations and needs an offline lookup table [32]. Based on FDA, the fundamental duty modulation (FDM) is proposed to minimize rms currents and extend ZVS ranges with a simple control structure [17]. However, rms currents are not optimized at light load because only the fundamental component is considered in FDM; see Fig. 1(b). The FDA-based multiorder reactive-current suppression (MRS) method can suppress the reactive current of fundamental and harmonic frequency [16]. However, as illustrated in Fig. 1(c), MRS loses its effectiveness and has a limited power range at heavy load when the voltage conversion ratio is low.

The optimization of inductor rms currents is an important point for DAB converters [15]. First, the power losses of the DAB converters are mainly composed of conduction losses, core losses, and switching losses. Optimizing inductor rms currents can reduce power losses and improve transmission efficiency. Meanwhile, the smaller sizes of magnetic components and lower current stresses of power devices can be achieved by suppressing the inductor rms current [30]. If rms currents are large, then chronic high current stresses and unsatisfactory temperatures caused by power losses can induce component failure [33]. The output voltage ripple, determining the design of output filter capacitors, is another point that is supposed to be concerned especially for ripple-sensitive renewable energy sources or power loads [34], [35]. Higher output voltage ripples require larger capacitance, leading to lower power density and higher cost [36]. The traditional design of the output filter capacitor is based on the estimation method by peak output voltage ripple [37].

A lot of studies have been developed to suppress the output voltage ripples. Various topologies, such as modular and current-fed dc–dc converters, have been proposed to reduce the output ripples [38], [39], [40], [41]. As for the two-stage single-phase converter, the virtual impedance, notch filter, and proportional-resonant control are used to suppress the double line-frequency fluctuation for lower required capacitances [16], [42], [43]. However, the controller design is complex and the high-frequency voltage ripples need to be optimized [44]. Notably, the double line-frequency fluctuation in the two-stage single-phase converter is also called low-frequency voltage ripple in some literature [16], [42], [43], but there are still existing high-frequency ripples in the single-stage DAB converters. The output current feedforward compensation strategy and slide-mode control are proposed to improve the dynamic performance of the DAB converter [44], [45], which can suppress the high-frequency voltage ripples indirectly by reducing phase shift angle fluctuation. Nevertheless, these methods are based on the SPS modulation and the high-frequency output voltage ripples can be suppressed further by advanced modulation methods. The high-frequency output voltage ripples with the DPS modulation are smaller than the SPS modulation from the experimental results [46]. However, no mathematical analysis of the high-frequency output voltage ripples is conducted in [46]. Therefore, a DAB model representing the output voltage ripples should be built to optimize the output filter capacitor of DAB converters.

This study proposes a composite duty modulation (CDM) scheme of DAB converters to reduce their output voltage ripples and inductor rms currents and improve converter efficiency, which can overcome the limits of the FDM scheme under light load and MRS strategy under heavy load. The output voltage ripples and inductor currents of DAB converters are represented by a generalized averaging model considering the second harmonic component. The improved CDM (I-CDM) scheme has also been proposed to optimize CDM performance. The main contributions of this study are listed as follows.

1) The output voltage ripple is hard to be represented by the traditional frequency model. The generalized averaging model of DAB considering the second harmonic component is built to represent the inductor currents and output voltage ripples for modulation scheme design and parametric analysis. The impact of harmonic components on the inductor currents and output voltage ripples is also analyzed.

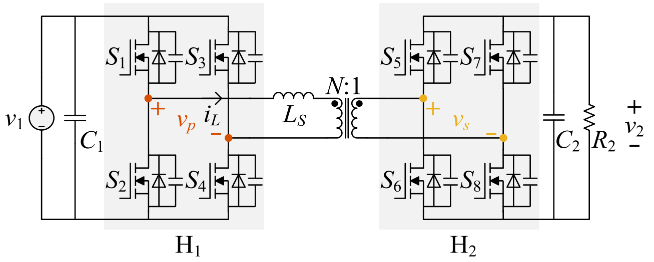

Fig. 2. Topology of a DAB converter.

2) A CDM scheme of DAB converters is proposed to optimize inductor rms currents, output voltage ripples, and transmission efficiency over broad voltage conversion ratios and power ranges, which can be realized simply without complex modeling processes, offline calculation, and additional current information.
3) The CDM scheme is modified to I-CDM for performance optimization when the voltage conversion ratio approaches unity under light load. The proposed modulation methods can be applied to the conditions of reverse power flow or changed loads. The output capacitances with CDM or I-CDM schemes are reduced by around 75% compared with the SPS method at light load. The proposed I-CDM scheme can reach the maximum efficiency of 98.4% from experimental results.

II. DAB Converter Model Considering the Second Harmonic Component

A. *Principle of DAB Converters*

The topology of a DAB converter is shown in Fig. 2. The DAB converter comprises two H-bridges, a high-frequency transformer, two filter capacitors, and an auxiliary inductor. Switches S$_1$–S$_4$ and S$_5$–S$_8$ form primary H-bridge H$_1$ and secondary H-bridge H$_2$, which generate ac voltages v_p and v_s, respectively. The transformer turns ratio is N:1. C_1 and C_2 are the input and output filter capacitors, respectively. Equivalent inductance L_S comprises the auxiliary inductance and transformer leakage inductance. R_2 is the output load. v_1, v_2, and i_L are the primary dc voltage, secondary dc voltage, and inductor current, respectively.

The gating signals and transformer voltage waveforms of a DAB converter are depicted in Fig. 3. Switching frequency $f_s = 1/T_s$, where T_s is the switching period. s_1–s_8 are the gating signals of switches S_1–S_8 with 50% duty ratio. $\bar{s}_1 - \bar{s}_8$ are the complementary gating signals of s_1–s_8. In the case of TPS modulation, switching functions are determined by three control arguments: d_1, d_2, and ϕ, which respectively describe the duty ratios of v_p, v_s, and the PS ratio between their fundamental components with respect to $T_s/2$. SPS, DPS, and EPS modulations can be taken as special cases of TPS. SPS modulation can be achieved when $d_1 = d_2 = 1$, DPS modulation can be achieved when $d_1 = d_2$, and EPS modulation can be achieved when $d_1 = 1$ or $d_2 = 1$.

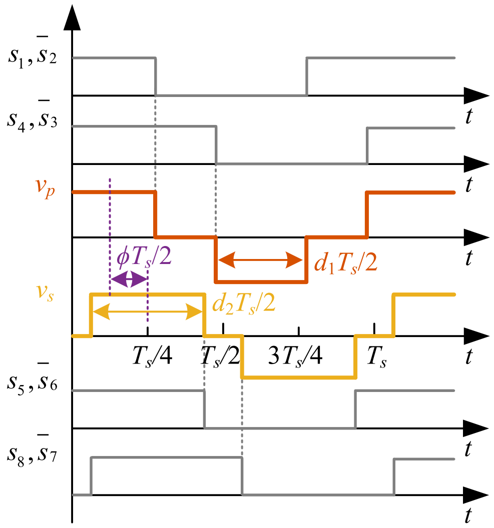

Fig. 3. Gating signals and transformer voltage waveforms of a DAB converter.

The switching function $g_1(t)$ of H$_1$ is

$$g_1(t)=\begin{cases}1, & 0 \le \tau < (1-2\phi+d_1)T_s/4 \\ & \text{or}(5-2\phi-d_1)T_s/4 \le \tau < T_s \\ 0, & (1-2\phi+d_1)T_s/4 \le \tau < (3-2\phi-d_1)T_s/4 \\ & \text{or}(3-2\phi+d_1)T_s/4 \le \tau < (5-2\phi-d_1)T_s/4 \\ -1, & (3-2\phi-d_1)T_s/4 \le \tau < (3-2\phi+d_1)T_s/4\end{cases} \tag{1}$$

where the time interval $\tau \in [t - T_s, t]$. The switching function $g_2(t)$ of H$_2$ is

$$g_2(t) = \begin{cases}1, & (1-d_2)T_s/4 \le \tau < (1+d_2)T_s/4 \\ & 0 \le \tau < (1-d_2)T_s/4, \\ 0, & (1+d_2)T_s/4 \le \tau < (3-d_2)T_s/4, \\ & \text{or}(3+d_2)T_s/4 \le \tau < T_s \\ -1, & (3-d_2)T_s/4 \le \tau < (3+d_2)T_s/4.\end{cases} \tag{2}$$

The state-space equations of a DAB converter can be derived as follows:

$$\begin{cases}di_L/dt = (g_1v_1 - Ng_2v_2)/L_S \\ dv_2/dt = (-v_2/R_2 + Ng_2i_L)/C_2\end{cases} \tag{3}$$

where v_1, v_2, and i_L are the input voltage, output voltage, and inductor current, respectively.

B. *DAB Converter Model Considering the Second Harmonic Component*

The generalized averaging model can be applied to model the DAB converter, and the nonlinear and time-varying state-space equations can be processed. The even harmonic components of the inductor current are 0 through Fourier analysis [18], [47]. The odd harmonic components of the output voltage are 0 through the same analysis. Therefore, in this study, the first harmonic component $\langle i_L \rangle_1$ of i_L and the zeroth $\langle v_2 \rangle_0$ and second harmonic components $\langle v_2 \rangle_2$ of v_2 are considered to model the DAB converter.

The kth complex Fourier coefficient of the signal $x(\tau)$ is

$$\langle x\rangle_k(t) = (1/T_s)\int_{t-T_s}^{t} x(\tau)e^{-jk\omega_s\tau}d\tau. \tag{4}$$

Therefore, the zeroth, first, and second coefficients of switching functions $g_1(\tau)$ and $g_2(\tau)$ can be derived from (4)

$$\begin{cases}\langle g_1\rangle_0 = \langle g_2\rangle_0 = \langle g_1\rangle_2 = \langle g_2\rangle_2 = 0\\ \langle g_1\rangle_1 = 2\sin(\phi\pi)\sin(d_1\pi/2)/\pi\\ \quad -j2\cos(\phi\pi)\sin(d_1\pi/2)/\pi\\ \langle g_2\rangle_1 = -j2\sin(d_2\pi/2)/\pi\end{cases} \tag{5}$$

where the zeroth and second coefficients are 0 and are consistent with the result in [18].

The different coefficients of the product of two variables g and x can be calculated as follows:

$$\begin{cases}\langle gx\rangle_1^R = \langle g\rangle_0\langle x\rangle_1^R + \langle g\rangle_1^R\langle x\rangle_0 + \langle g\rangle_1^R\langle g\rangle_2^R + \langle g\rangle_1^I\langle x\rangle_2^I\\ +\langle g\rangle_2^R\langle x\rangle_1^R + \langle g\rangle_2^I\langle x\rangle_1^I\\ \langle gx\rangle_1^I = \langle g\rangle_1^I\langle x\rangle_0 + \langle g\rangle_0\langle x\rangle_1^I - \langle g\rangle_2^R\langle x\rangle_1^I + \langle g\rangle_1^R\langle x\rangle_2^I\\ +\langle g\rangle_2^I\langle x\rangle_1^R - \langle g\rangle_1^I\langle x\rangle_2^R\\ \langle gx\rangle_2^R = \langle g\rangle_2^R\langle x\rangle_0 - \langle g\rangle_1^I\langle x\rangle_1^I + \langle g\rangle_1^R\langle x\rangle_1^R + \langle g\rangle_0\langle x\rangle_2^R\\ \langle gx\rangle_2^I = \langle g\rangle_2^I\langle x\rangle_0 + \langle g\rangle_1^R\langle x\rangle_1^I + \langle g\rangle_0\langle x\rangle_2^I + \langle g\rangle_1^I\langle x\rangle_1^R\end{cases} \tag{6}$$

where superscripts "R" and "I" mean the real and imaginary parts of the corresponding variables, respectively.

Hence, from (3)–(6), the DAB converter model considering the second harmonic can be acquired

$$\begin{cases}\frac{d\langle i_L\rangle_1^R}{dt} = \omega_s\langle i_L\rangle_1^I - \frac{N\langle g_2\rangle_1^I\langle v_2\rangle_2^I}{L_S} + \frac{\langle g_1\rangle_1^R\langle v_1\rangle_0}{L_S}\\ \frac{d\langle i_L\rangle_1^I}{dt} = -\omega_s\langle i_L\rangle_1^R - \frac{N\langle g_2\rangle_1^I\langle v_2\rangle_0}{L_S} + \frac{N\langle g_2\rangle_1^I\langle v_2\rangle_2^R}{L_S} + \frac{\langle g_1\rangle_1^I\langle v_1\rangle_0}{L_S}\\ \frac{d\langle v_2\rangle_0}{dt} = \frac{2N\langle g_2\rangle_1^I\langle i_L\rangle_1^I}{C_2} - \frac{\langle v_2\rangle_0}{R_2C_2}\\ \frac{d\langle v_2\rangle_2^R}{dt} = -\frac{N\langle g_2\rangle_1^I\langle i_L\rangle_1^I}{C_2} - \frac{\langle v_2\rangle_2^R}{R_2C_2} + 2\omega_s\langle v_2\rangle_2^I\\ \frac{d\langle v_2\rangle_2^I}{dt} = \frac{N\langle g_2\rangle_1^I\langle i_L\rangle_1^R}{C_2} - 2\omega_s\langle v_2\rangle_2^R - \frac{\langle v_2\rangle_2^I}{R_2C_2}\end{cases} \tag{7}$$

where $\omega_s = 2\pi f_s$. The dc and second components of i_L and the first harmonic component of v_2 are 0 and omitted herein [18].

Because $\langle V_1\rangle_0 = V_1$ and $\langle V_2\rangle_0 = V_2$ in the steady state, where V_1 and V_2 are dc components of input and output voltage, respectively [47]. Therefore, the steady-state values of i_L and v_2 can be calculated as follows:

$$\begin{cases}\langle I_L\rangle_1^R = -N\langle g_2\rangle_1^I V_2/(\omega_s L_S) + \langle g_1\rangle_1^I V_1/(\omega_s L_S)\\ \langle I_L\rangle_1^I = -\langle g_1\rangle_1^R V_1/(\omega_s L_S)\\ \langle V_2\rangle_2^R = -[N\langle g_2\rangle_1^I R_2(-\langle g_1\rangle_1^R V_1 - 2\omega_s R_2C_2\langle g_1\rangle_1^I V_1\\ \quad +2N\omega_s R_2C_2\langle g_2\rangle_1^I V_2)]/[\omega_s L_S(1+4C_2^2R_2^2\omega_s^2)]\\ \langle V_2\rangle_2^I = -[N\langle g_2\rangle_1^I(-R_2\langle g_1\rangle_1^R V_1 + NR_2\langle g_2\rangle_1^I V_2\\ \quad +2\omega_s R_2^2C_2\langle g_1\rangle_1^R V_1)]/[\omega_s L_S(1+4C_2^2R_2^2\omega_s^2)].\end{cases} \tag{8}$$

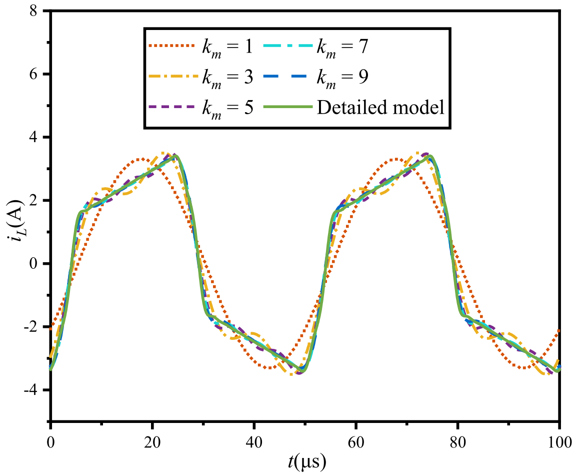

Fig. 4. Inductor current comparison between the frequency model ($k_m = 1$, 3, 5, 7, and 9) and detailed model calculated with circuit parameters in Table I.

TABLE I
CIRCUIT PARAMETERS OF A 1 KW DAB CONVERTER PROTOTYPE

Symbol	Item	Quantity
N:1	transformer turns ratio	2:1
M	voltage conversion ratio	0.4–1
V_1	input voltage	150 V
V_2	output voltage	30–75 V
P_{max}	maximum power	1.0 kW
f_s	switching frequency	20 kHz
L_S	equivalent inductance	205.35 μH
C_2	output filter capacitor	208.55 μF

Notably, the inductor current ripple is much larger than the output voltage ripple, and only the dc component of the output voltage is used to calculate the inductor current for simplicity.

The fundamental component of i_L and the second harmonic component of v_2 can be derived as follows:

$$\begin{cases}I_{L\_1} = \sqrt{\left(2\langle I_L\rangle_1^R\right)^2 + \left(2\langle I_L\rangle_1^I\right)^2}\\ V_{2\_2} = \sqrt{\left(2\langle V_2\rangle_2^R\right)^2 + \left(2\langle V_2\rangle_2^I\right)^2}.\end{cases} \tag{9}$$

Output power P_o can be computed as follows:

$$P_o = \frac{2NV_1V_2}{\omega_s L_S}\langle g_1\rangle_1^R(-\langle g_2\rangle_1^I). \tag{10}$$

C. Impact of Harmonic Components

The inductor current under various harmonic components can be calculated by the traditional frequency model from paper [18]. The inductor current comparison between the frequency model (k_m = 1, 3, 5, 7, and 9) and the detailed model are plotted in Fig. 4, where k_m is the maximum considered harmonic level. The detailed model is built on MATLAB/Simulink with circuit parameters in Table I. It is illustrated that the waveforms of the inductor current approach the detailed model when more harmonic components are considered. The amplitude spectrum of the inductor current is presented in Fig. 5. The spectrum

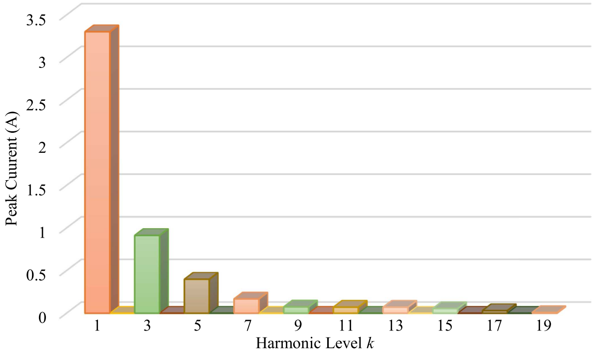

Fig. 5. Amplitude spectrum of the inductor current calculated with circuit parameters in Table I.

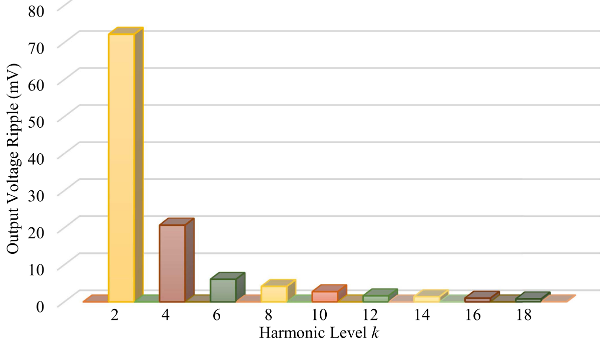

Fig. 6. Amplitude spectrum of the output voltage ripple calculated with circuit parameters in Table I.

reveals that the inductor current primarily consists of odd harmonics, with the fundamental component exhibiting the highest amplitude.

Because the traditional frequency model cannot represent the output voltage ripple [18], the detailed model from MATLAB/Simulink is used to acquire the amplitude spectrum of the output voltage ripple, as shown in Fig. 6. The output voltage ripple primarily consists of even harmonics, and the second component accounts for the majority.

The proposed DAB model, considering the second harmonic component, is used to calculate the output voltage. The output voltage comparison between the proposed model ($k_m = 1$ and 2) and the detailed model is shown in Fig. 7. The frequency of the output voltage ripple is twice the switching frequency. When only the fundamental component ($k_m = 1$) of state variables is considered, the output voltage ripple cannot be observed. If the second harmonic component is taken into account, the output voltage ripple can be represented. Therefore, at least the second harmonic component should be considered for optimizing the output voltage ripples. When more harmonic components are considered, the results are closer to the detailed model. However, the complexity of the model increases sharply.

III. CDM OF A DAB CONVERTER

A. *Output Voltage Ripple Optimization*

The output voltage ripple can be optimized by Karush–Kuhn–Tucker (KKT) conditions [48]. The optimization problem is

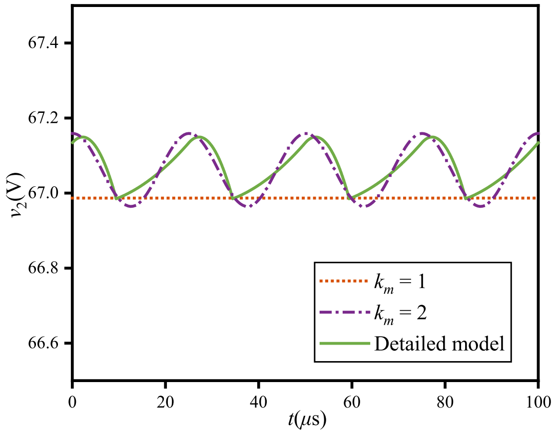

Fig. 7. Output voltage comparison between the proposed model ($k_m = 1$ and 2) and the detailed model calculated with circuit parameters in Table I.

formulated into the following standard form:

$$\begin{array}{c}\mathrm{Min}[V_{2\_2}(\mathbf{X})]^2\\ \mathrm{s.t.}\, P_o(\mathbf{X}) - P_b = 0, h_i(\mathbf{X}) \le 0\end{array} \tag{11}$$

where $\mathbf{X} = (\langle g_1\rangle_1^R, \langle g_1\rangle_1^I, \langle g_2\rangle_1^I)$ and $P_b = 8NV_1V_2/(\pi^2\omega_s L_s)$. KKT conditions are expressed as follows:

$$\begin{aligned}&L(\mathbf{X},\lambda,\boldsymbol{\mu}) = [V_{2\_2}(\mathbf{X})]^2 + \lambda[P_o(\mathbf{X}) - P_b]\\ &+\mu_1\left(\langle g_1\rangle_1^R - \frac{2}{\pi}\right) + \mu_2\left(-\langle g_1\rangle_1^I - \frac{2}{\pi}\right) + \mu_3\left(-\langle g_2\rangle_1^I - \frac{2}{\pi}\right)\end{aligned}$$

$$\mathrm{s.t.}\begin{cases}\frac{\partial L}{\partial\langle g_1\rangle_1^R} = 0, \frac{\partial L}{\partial\langle g_1\rangle_1^I} = 0, \frac{\partial L}{\partial\langle g_2\rangle_1^I} = 0\\ \lambda \ne 0\\ P_o(\mathbf{X}) - P_b = 0\\ \mu_1 \ge 0, \mu_2 \ge 0, \mu_3 \ge 0,\\ \langle g_1\rangle_1^R - \frac{2}{\pi} \le 0, -\langle g_1\rangle_1^I - \frac{2}{\pi} \le 0, -\langle g_2\rangle_1^I - \frac{2}{\pi} \le 0\\ \mu_1(\langle g_1\rangle_1^R - \frac{2}{\pi}) = 0\\ \mu_2(-\langle g_1\rangle_1^I - \frac{2}{\pi}) = 0\\ \mu_3(-\langle g_2\rangle_1^I - \frac{2}{\pi}) = 0\end{cases} \tag{12}$$

where L is the Lagrangian function and λ and $\mu = (\mu_1, \mu_2, \mu_3)$ are KKT multipliers. Optimal control parameters $(\langle g_1\rangle_{1\mathrm{opt}}^R, \langle g_1\rangle_{1\mathrm{opt}}^I, \langle g_2\rangle_{1\mathrm{opt}}^I)$ can be derived to minimize the output voltage ripple, which is

$$\begin{aligned}\langle g_1\rangle_{1\mathrm{opt}}^R &= -\omega_s L_S P_o/(2NV_1V_2\langle g_2\rangle_{1\mathrm{opt}}^I)\\ \langle g_1\rangle_{1\mathrm{opt}}^I &= NV_2\langle g_2\rangle_{1\mathrm{opt}}^I/V_1.\end{aligned} \tag{13}$$

From (5), (13) is rewritten as follows:

$$\begin{cases}\cos(\phi\pi)\sin(d_1\pi/2) = M\sin(d_2\pi/2)\\ P_{ob} = \sin(d_1\pi/2)\sin(d_2\pi/2)\sin(\phi\pi)\end{cases} \tag{14}$$

where M is the voltage conversion ratio and equals NV_2/V_1. $P_{ob} = P_o/P_b$. The output voltage ripple can be minimized if (14) is satisfied.

B. Proposed CDM

Three control variables are involved in TPS modulation. However, only two equations exist in (14). Another constraint condition should be considered. Equation (9) can be rearranged as follows:

$$I_{L\_1} = \frac{4V_1}{\pi\omega_s L_S}\sqrt{\begin{array}{l}[M\sin(d_2\pi/2) - \cos(\phi\pi)\sin(d_1\pi/2)]^2\\ +[\sin(\phi\pi)\sin(d_1\pi/2)]^2\end{array}}. \tag{15}$$

Equation (15) can also be used to achieve the minimum inductor rms current, which is unified to optimize I_{L_1} and V_{2_2}. Solving the constrained optimization problem of the inductor rms current, I_{L_1} is minimized when $d_2 = 1$ [17]. FDM effectively reduces the fundament frequency current. Control variables are derived as follows:

$$\begin{cases} d_1 = 2\arcsin[M/\cos(\phi\pi)]/\pi \\ d_2 = 1. \end{cases} \tag{16}$$

However, the third harmonic component is increased at a low power level through FDM, and the inductor current can be optimized further. $d_1 = Md_2$ is used in the MRS strategy [16], which has a lower inductor rms current than FDM at a low power level. Control variables are computed as follows:

$$\begin{cases} d_1 = 2\sqrt{3}M\phi/\sqrt{1-M^2} \\ d_2 = 2\sqrt{3}\phi/\sqrt{1-M^2}. \end{cases} \tag{17}$$

The weakness of the MRS strategy is the limited power range and higher inductor rms current than FDM at a high-power level. The advantages of FDM at a high-power level and MRS at a low-power level can be composited. The power intersection point can be acquired by equating the power and rms current of FDM and MRS from (10) and (15). At the intersection point, control variables d_{1i}, d_{2i}, and ϕ_i are as follows:

$$\begin{cases} d_{1i} = M \\ d_{2i} = 1 \\ \phi_i = \arccos[M/\sin(M\pi/2)]/\pi. \end{cases} \tag{18}$$

ϕ is positively proportional to the transferred power. When $0 \leq \phi < \phi_i$, (17) is used to modulate the DAB converter. When $\phi_i \leq \phi \leq 0.5$, (16) is used. That is the basic idea of CDM.

C. Proposed I-CDM

In Fig. 1, when M approaches 1, FDM, MRS, and CDM have slightly higher rms currents than SPS at a low power level ($0 \leq \phi < \phi_i$), which is illustrated in Section IV-D. This is because the first equation of (14) is based on the first and second harmonic levels. Plotting the relationship of d_2 and ϕ under the minimum rms current [49], as shown in Fig. 8, the following equation can be acquired:

$$d_2 = 2\phi/(1 - M) \tag{19}$$

which is along with $d_1 = M\,d_2$ to improve CDM

$$\begin{cases} d_1 = 2M\phi/(1-M) \\ d_2 = 2\phi/(1-M). \end{cases} \tag{20}$$

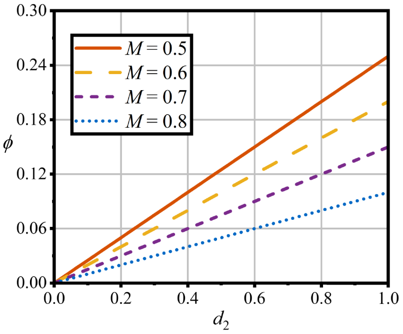

Fig. 8. d_2 and ϕ under minimum inductor rms current.

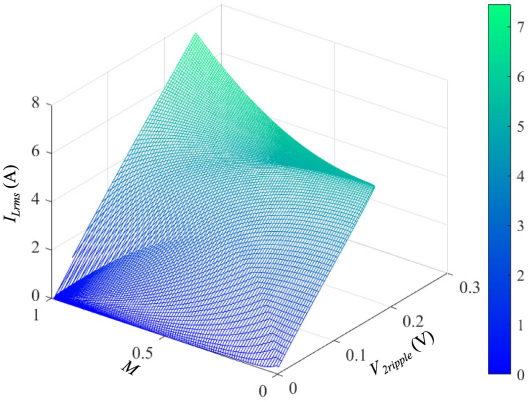

Fig. 9. Relationship between the voltage ripple and inductor rms current under different voltage conversion ratios M calculated with circuit parameters in Table I.

When $0 \leq \phi < \phi_i$, (20) is used to modulate the DAB converter. When $\phi_i \leq \phi \leq 0.5$, (16) is used. That is the basic idea of the I-CDM.

Notably, the inductor rms current is mainly positively correlated with the output voltage ripple, as shown in Fig. 9. Therefore, when the constraint of the minimum output voltage ripple is added, it also keeps the inductor rms current at a low level. A lower inductor rms current will induce higher conversion efficiency [15], indicating that the optimization objectives of the proposed CDM and I-CDM are not conflicting. The proposed methods can optimize the output voltage ripple further while keeping a low inductor rms current.

D. Solution for M > *1*

The case of $M > 1$ should be considered for broad application. The inverse power flow that is transferred from the secondary side to the primary side with $M \leq 1$ is equal to the positive power flow from the primary side to the secondary side with $M > 1$ [26]. Hence, the optimized modulation scheme CDM for $M > 1$ can be acquired

$$\begin{array}{ll} 0 \leq \phi < \phi_i', & \begin{cases} d_1 = 2\sqrt{3}M\phi/\sqrt{M^2-1} \\ d_2 = 2\sqrt{3}\phi/\sqrt{M^2-1} \end{cases} \\ \phi_i' \leq \phi \leq 0.5, & \begin{cases} d_1 = 1 \\ d_2 = 2\arcsin\{1/[M\cos(\phi\pi)]\}/\pi \end{cases} \end{array} \tag{21}$$

TABLE II
MODULATION VARIABLES AND RMS CURRENT OF CDM AND I-CDM OF THE 1 kW DAB CONVERTER PROTOTYPE WHEN $P_n = 0.1$ AND $M = 4$

Optimized schemes	Items	Quantity
CDM	d_1	0.619
	d_2	0.155
	ϕ	0.173
	I_{Lrms}	3.158 A
I-CDM	d_1	0.517
	d_2	0.129
	ϕ	0.194
	I_{Lrms}	2.942 A

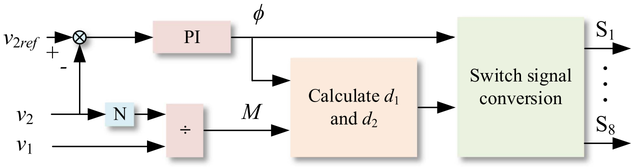

Fig. 10. Control structure of a close loop for the DAB converter with the CDM strategy.

where ϕ_i' can be computed as follows:

$$\phi_i' = \arccos\{1/[M\sin(\pi/2M)]\}/\pi. \tag{22}$$

The optimized modulation scheme I-CDM for $M > 1$ can also be obtained.

$$\begin{aligned} &0 \le \phi < \phi_i', \begin{cases} d_1 = 2M\phi/(M-1) \\ d_2 = 2\phi/(M-1) \end{cases} \\ &\phi_i' \le \phi \le 0.5, \begin{cases} d_1 = 1 \\ d_2 = 2\arcsin\{1/[M\cos(\phi\pi)]\}/\pi. \end{cases} \end{aligned} \tag{23}$$

The transmission power of CDM and I-CDM for the same ϕ is different for $M > 1$ under light load. However, it is usually to compare the inductor rms current at the same power rating. There are various combinations of modulation variables to transfer the same required power. When the normalized power $P_n = 0.1$ and $M = 4$, the modulation variables and inductor rms current of CDM and I-CDM of the 1 kW DAB converter prototype are listed in Table II. It illustrates that the I-CDM can reduce 6.84% of inductor rms current than CDM, and the modulation variables are different between CDM and I-CDM when transferring the same power.

E. Close-Loop Control Structure

Fig. 10 illustrates the control structure of the close loop for the DAB converter using the CDM strategy. Output voltage v_2 is compared with reference voltage $v_{2\text{ref}}$ and regulated by the single close loop PI controller, which produces ϕ. M can be calculated by the voltage information or set as a constant for a fixed output voltage. ϕ and M are used to calculate d_1 and d_2 from (16) and (17). Finally, ϕ, d_1, and d_2 are conversed to regulate the eight switches of DAB converters. The control structure of the close loop with the I-CDM strategy is similar to CDM and omitted herein.

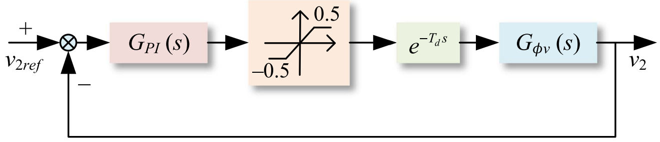

Fig. 11. Block diagram of the feedback control.

F. Design of PI Controller Parameters

The proportional–integral (PI) feedback control is used to control the DAB converter, and the block diagram is shown in Fig. 11, which comprises PI compensator $G_{\text{PI}}(s)$, amplitude limiter, delay link $e^{-T_d s}$, and control-to-output transfer function $G_{\phi v}(s)$ [11].

The open-loop forward path transfer function $G_{\text{open}}(s)$ can be used to design controller parameters

$$G_{\text{open}}(s) = G_{\text{PI}}(s)G_{\phi v}(s)e^{-T_d s}. \tag{24}$$

The PI compensator $G_{\text{PI}}(s) = k_P + k_I/s$ is used to optimize the steady-state errors. The small-signal control-to-output transfer function can be derived from the DAB model [11]

$$G_{\phi v}(s) = \frac{\Delta v_2}{\Delta\phi} = \frac{NV_1R_2(1-2\phi)}{2f_s(sC_2R_2+1)}. \tag{25}$$

In classical control theory, it is proposed that the forward path of a control system should have unity gain and a specified phase margin φ_m at the crossover frequency ω_c. This approach helps ensure stability and robustness in the control system design. Therefore, k_P and k_I can be derived as follows [44]:

$$\begin{cases} \left|\left(k_P + \frac{k_I}{j\omega_c}\right)\frac{NV_1R_2(1-2\phi)}{2f_s(j\omega_c C_2R_2+1)}e^{-j\omega_c T_d}\right| = 1 \\ \angle\left[\left(k_P + \frac{k_I}{j\omega_c}\right)\frac{NV_1R_2(1-2\phi)}{2f_s(j\omega_c C_2R_2+1)}e^{-j\omega_c T_d}\right] = -\pi + \varphi_m. \end{cases} \tag{26}$$

IV. OPERATIONAL CHARACTERISTICS

A. Analysis of the Influence Factors of Optimized Output Voltage Ripples

From (9) and (13), the output voltage ripple $V_{2\text{ripple}}$ under optimal conditions can be derived as follows:

$$V_{2\text{ripple}} \approx V_{2\_2} = \sqrt{\frac{V_2^2}{1 + 4C_2^2\omega_s^2V_2^4/P_o^2}} \tag{27}$$

where the output voltage ripple is related to P_o, C_2, V_2, and f_s. The influences of different factors on the output voltage ripple of the DAB converter are investigated with the circuit parameter listed in Table I, as shown in Fig. 12. The output voltage ripple is positively proportional to the transmission power, whereas the output capacitance, output dc voltage, and switching frequency have an inverse relationship with the output voltage ripple. Therefore, the DAB converter model considering the second harmonic component can be used to optimize the design of output filter capacitors from (9) and (27).

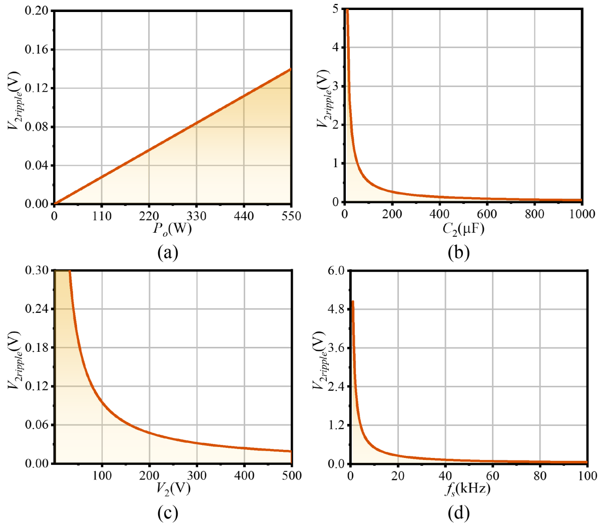

Fig. 12. Influence factors of output voltage ripples calculated with circuit parameters in Table I. (a) Power rating. (b) Output filter capacitance. (c) Output dc voltage. (d) Switching frequency.

B. Analysis of the Influence Factors of Inductor RMS Currents

From (15), the inductor rms current is associated with control variables (d_1, d_2, and ϕ), M, V_1, f_s, and L_S. Various modulation schemes have different control variables under the same load condition and M, leading to different optimization effects, which are discussed in Section IV-D. The inductor rms current has a linear proportion with V_1, f_s, and L_S from (15), the same as many studies [16], [17], [18], [19], [20], [21].

C. Output Voltage Ripple Comparison With Various Modulation Methods

The calculation equations of output voltage ripples are not provided in [16], [17], [18], [19], [20], and [21]. Therefore, the output voltage ripple is evaluated by (9), and the output voltage ripple comparison among different modulation schemes of the 1 kW DAB converter prototype is shown in Fig. 13. Output voltage ripples are associated with inductor rms currents, so the suppression strategies of rms current are also effective in suppressing output voltage ripples. SPS modulation has poor performance at light load. FDM loses its effectiveness at light load because only the fundamental component is considered in FDM. MRS can suppress voltage ripples at light load. However, MRS cannot realize the maximum power transmission when M is small. The effectiveness of suppressing the output voltage ripple with GOC decreases at light loads when M increases. The proposed CDM and I-CDM can achieve power transmission at the whole power range and voltage conversion ratio. The proposed methods perform better than other modulation methods using FDA. Meanwhile, the proposed methods have slightly lower output voltage ripples than GOC under light load. Notably, GOC is based on TDA, which requires complex offline computation of various working modes [16]. However, FDA is used in the proposed methods, which can be applied to the whole operation range without mode classification and alleviates the modeling complexity [17], [18].

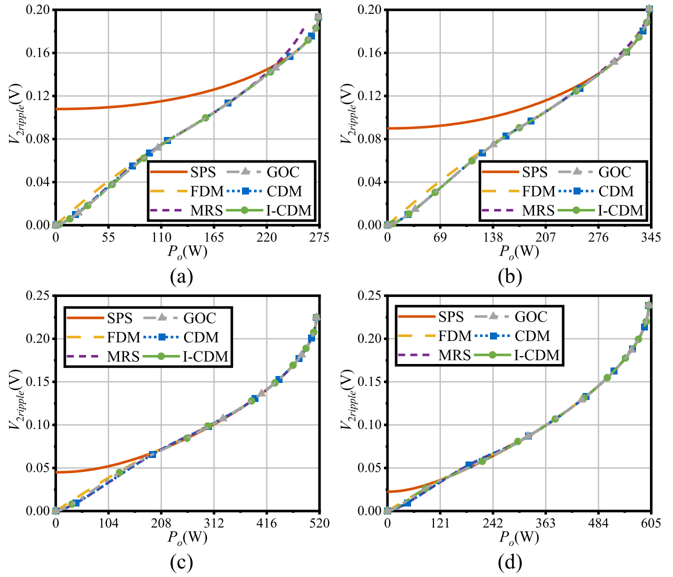

Fig. 13. Output voltage ripples of different modulation strategies of the 1 kW DAB converter prototype for (a) $M = 0.4$, (b) $M = 0.5$, (c) $M = 0.75$, (d) $M = 0.875$.

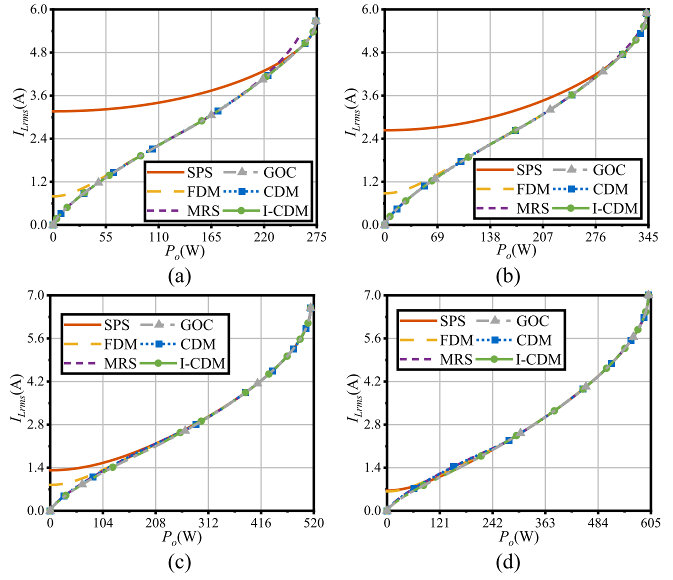

Fig. 14. Inductor rms currents of different modulation strategies of the 1 kW DAB converter prototype for (a) $M = 0.4$, (b) $M = 0.5$, (c) $M = 0.75$, (d) $M = 0.875$.

D. Inductor RMS Current Comparison With Various Modulation Methods

In Fig. 14, the inductor rms currents of different modulation strategies of the 1 kW DAB converter prototype are plotted, which are calculated based on accurate time-domain-based numerical analysis [25], [26]. SPS modulation has the highest inductor rms current during a light-load condition. FDM achieves lower rms current than SPS. However, the rms current of FDM during a light-load condition can be reduced. MRS maintains low rms currents over broad power ranges. Nevertheless, MRS cannot realize low rms currents when M is away from 1 and full

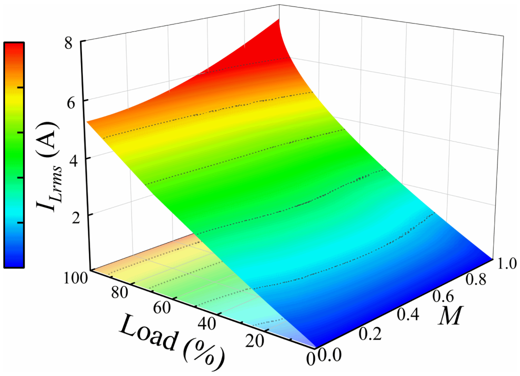

Fig. 15. Inductor rms currents of CDM and I-CDM of the 1 kW DAB converter prototype.

power operation. GOC has better performance in suppressing the rms current than FDM and MRS. However, complex mode analysis and solution procedures are needed. The proposed CDM method can effectively reduce rms current levels for different power ranges and M. FDM, MRS, and CDM have slightly higher rms currents than SPS when voltage conversion ratios are close to 1 at light-load conditions, as only low harmonic components are considered in these methods. To solve the unsatisfactory effect when M approaches unity at light load, I-CDM is put forward. Fig. 14 illustrates that I-CDM has better performance in suppressing inductor rms currents than SPS, FDM, MRS, and CDM. The difference between CDM and I-CDM is trivial and they are almost overlapped in Fig. 15. Notably, when the load approaches the maximum transmission power $P_{\max} = NV_1V_2/(8f_sL_S)$, most modulation methods switch into the SPS modulation with $d_1 = d_2 = 1$ and $\phi = 0.5$. Otherwise, the maximum power transmission cannot be realized. Therefore, the differences of most modulation methods at heavy loads are not significant [17], [50].

E. Comparison With the Case Considering the Third Harmonic Component

The model considering the third harmonic component of the DAB converter is derived in Appendix A. Because the formulae of rms current and output voltage ripple considering the third harmonic component are very complex from (30) to (33), it is hard to acquire an analytical solution to the optimization problem. Therefore, the PSO is used to find the optimal numerical solution, as shown in Appendix B. Notably, the PSO method herein optimizes the inductor current and output voltage ripple simultaneously, which is different from the one in [32]. The inductor rms currents with FDM, CDM, I-CDM, and PSO considering the third harmonic component ($k_m = 3$) of the 1 kW DAB converter prototype are shown in Fig. 16. It is observed that FDM has a higher rms current than other modulations because only the fundamental component is considered in the optimization process. Because the first harmonic component of the inductor current and the second harmonic component of the output voltage ripple, which are the main components of the inductor current and output voltage ripple, are optimized in CDM, CDM has better performance than FDM. Meanwhile, the effectiveness of CDM and PSO considering the third harmonic component is similar, and I-CDM has the lowest inductor rms current over the whole operating range due to the improvement at light load. Moreover, the CDM and I-CDM can realize online calculations for practical applications. Therefore, the CDM and I-CDM are easy to implement and have better performance than PSO considering the third harmonic component.

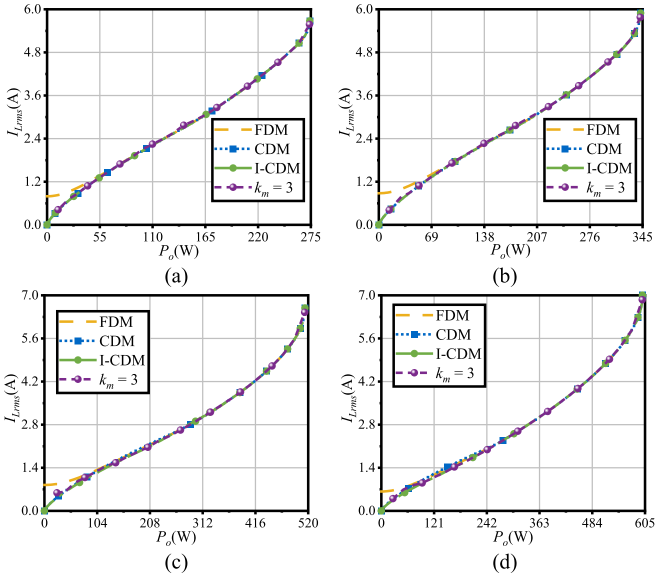

(a) (b) (c) (d)

Fig. 16. Inductor rms currents of FDM, CDM, I-CDM, and PSO considering the third harmonic component ($k_m = 3$) of the 1 kW DAB converter prototype. (a) $M = 0.4$. (b) $M = 0.5$. (c) $M = 0.75$. (d) $M = 0.875$.

F. ZVS Comparison With Various Modulation Methods

ZVS range is an important indicator of switching losses, and the ZVS boundary can be approximately evaluated by the direction and amplitude of the inductor current [17]. The ZVS range of the different modulation schemes at various loads and M are depicted. In Fig. 17, the ZVS area means all eight switches of the DAB converter can achieve ZVS, and the blank area indicates that only part of the switches turn ON with ZVS.

Fig. 17(a) is SPS scheme: S_5–S_8 of the secondary H-bridge lose ZVS at light-load and low voltage conversion ratio conditions, but the switches on the primary side realize ZVS.

Fig. 17(b) is FDM scheme: only S_3 and S_4 cannot realize ZVS under medium power range, but at a price of higher rms current at light-load.

Fig. 17(c) illustrates the ZCS region of S_3–S_6 using MRS and CDM, and other switches work on ZVS under light load. The inductor rms current can also be suppressed at this region to increase the system efficiency.

Fig. 17(d), although only S_1 and S_2 can achieve ZVS with I-CDM under light load, the other switches are in ZCS, which can also reduce the switching loss. Meanwhile, the rms current and output voltage ripples can be optimized with I-CDM over the whole power range. The ZVS performance of GOC is similar to I-CDM. Notably, the switching losses of GOC and I-CDM are slightly higher than CDM under light loads because the switches of ZVS have lower power loss than ZCS.

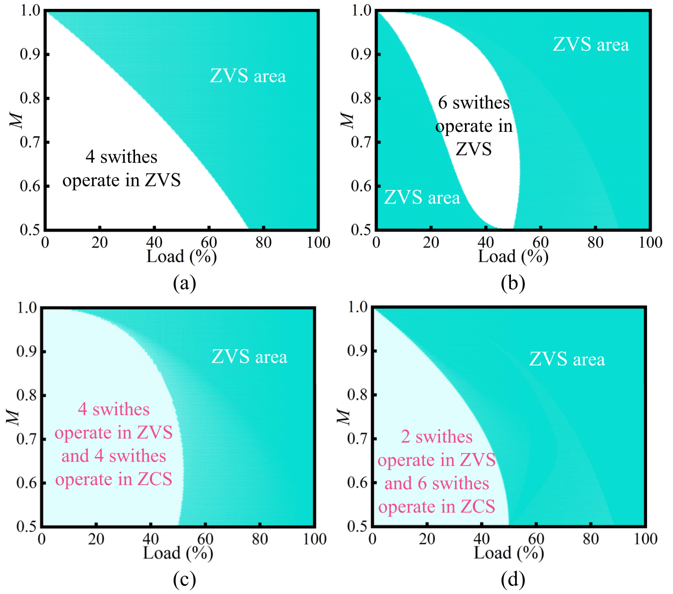

Fig. 17. ZVS range for different schemes. (a) SPS. (b) FDM. (c) MRS and CDM. (d) GOC and I-CDM.

TABLE III
PARAMETERS OF A 31.25 kW DAB CONVERTER PLATFORM

Symbol	Item	Quantity
N:1	transformer turns ratio	1:1
M	voltage conversion ratio	0.4–1
V_1	input voltage	1000 V
V_2	output voltage	400–1000 V
P_{max}	maximum power	31.25 kW
f_s	switching frequency	20 kHz
L_S	equivalent inductance	200 μH
C_2	output filter capacitor	500 μF

G. Case of the Proposed Methods With Larger Power

Table III lists the parameters of a 31.25 kW DAB converter platform, which is used as a module in the 10 kV/1 MVA solid-state transformer [16]. Notably, the maximum transmission power of the DAB converter is evaluated by $P_{\max} = NV_1V_2/(8f_sL_S)$, which changes at different working conditions. When $M = 1$, $P_{\max} = 31.25$ kW. With the DAB converter, the output voltage ripples of different modulation strategies are shown in Fig. 18. The proposed methods have better performance than other modulation methods with frequency-domain analysis. Additionally, the proposed methods have slightly lower output voltage ripples than GOC at light load. The inductor rms currents of different modulation strategies are depicted in Fig. 19. GOC performs better than FDM and MRS in suppressing the rms current. However, complex mode analysis and computational processes are needed. I-CDM has lower inductor rms currents than SPS, FDM, MRS, and CDM. The theoretical results of the 31.25 kW DAB converter platform are similar to that of the 1 kW DAB converter prototype. Therefore, the generality of the proposed method for the prototype with larger power is verified.

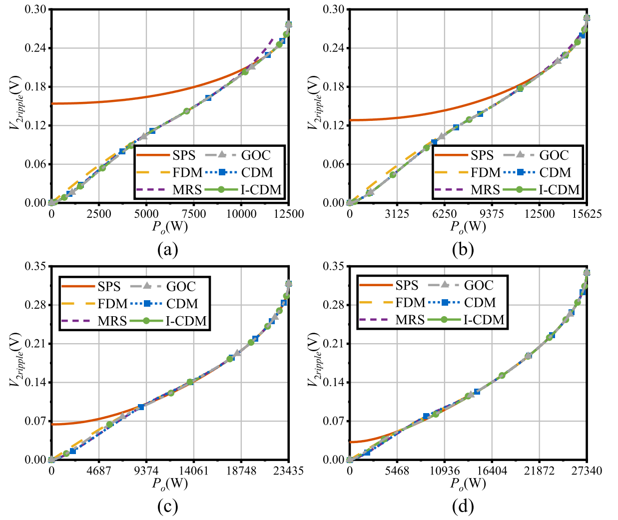

Fig. 18. Output voltage ripples of different modulation strategies of the 31.25 kW DAB converter platform for (a) $M = 0.4$, (b) $M = 0.5$, (c) $M = 0.75$, (d) $M = 0.875$.

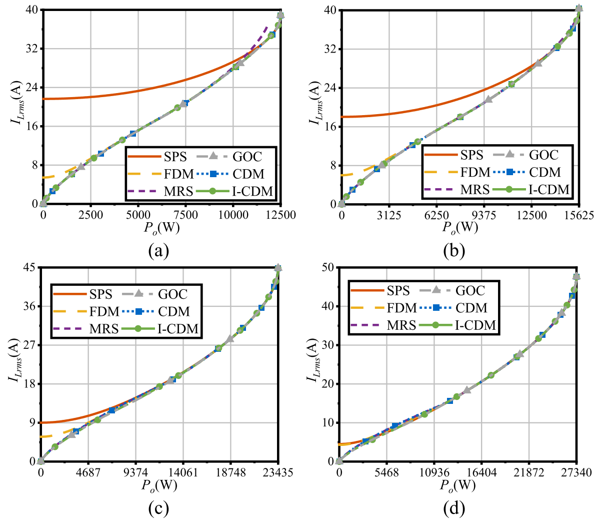

Fig. 19. Inductor rms currents of different modulation strategies of the 31.25 kW DAB converter platform for (a) $M = 0.4$, (b) $M = 0.5$, (c) $M = 0.75$, (d) $M = 0.875$.

The detailed model of a DAB converter is built on MATLAB/Simulink with circuit parameters in Table III. The working waveforms of SPS, CDM, and I-CDM at $M = 0.5$ and $P_n = 0.1$ are plotted in Fig. 20. SPS has large voltage ripples and inductor rms currents. The voltage ripples and inductor rms current are suppressed effectively by CDM and I-CDM. It means that the proposed methods can be used in high-power applications.

V. EXPERIMENTAL ANALYSIS

A 1.0 kW experimental prototype of a DAB converter (see Fig. 21) is built to verify the effectiveness of the proposed CDM scheme, with the circuit parameters listed in Table I. The input voltage is fixed at 150 V. The output voltage ranges from 30 to 75 V. The TMS320F28335 digital signal processor from

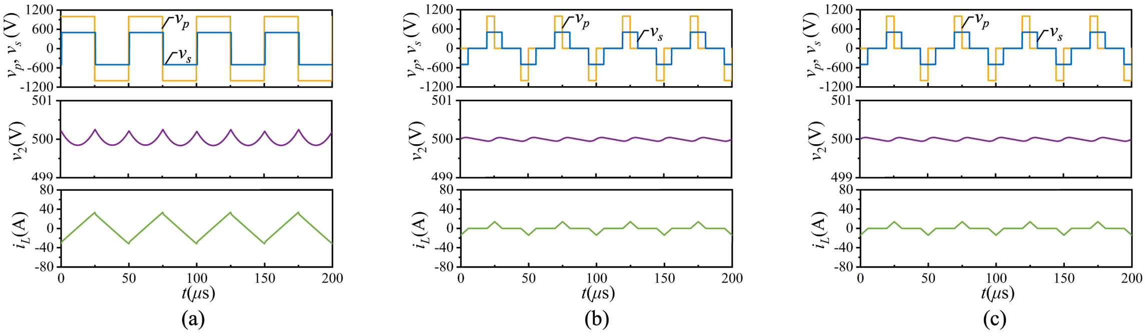

(a) (b) (c)

Fig. 20. Waveforms of the 31.25 kW DAB converter platform at $M = 0.5$ and $P_n = 0.1$. (a) SPS. (b) CDM. (c) I-CDM.

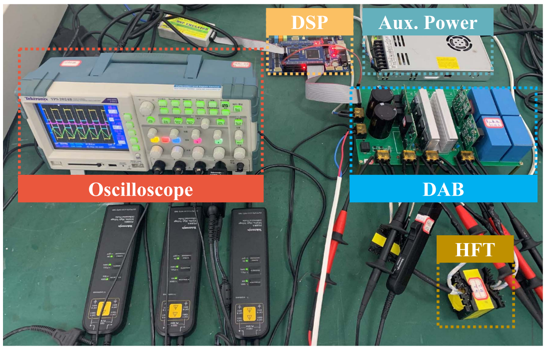

Fig. 21. Experimental prototype of a DAB converter.

TABLE IV
DESIGN PARAMETERS OF THE TRANSFORMER

Items	Quantity
core type	PQ50/50
material	PC95
primary turns	24
secondary turns	12
primary winding strands	300
secondary winding strands	600
wire diameter of the winding	0.1 mm

Texas Instruments is used to implement the proposed method. The silicon carbon MOSFET SCT3060AR from ROHM, with an ON-resistance of 60 mΩ, is selected as the switching device. The auxiliary power supplies the drive circuit. The transformer is designed by area product approach [51]. The design parameters of the transformer are shown in Table IV. To reduce the leakage inductance and improve efficiency, the transformer adopts sandwich winding, as shown in Fig. 22.

A. Output Voltage Ripple and Inductor RMS Current Comparison

The working waveforms of the 1 kW DAB converter prototype with the SPS, CDM, and I-CDM at $M = 0.5$ are shown in Figs. 23–25, respectively. P_n is the normalized power. For a light load when $P_n = 0.3$, the measured inductor rms currents using SPS, CDM, and I-CDM are 2.79, 1.77, and 1.76 A, respectively. From the perspective of voltage ripple, the values for SPS, CDM, and I-CDM are 85.4, 50.5, and 48.6 mV, respectively.

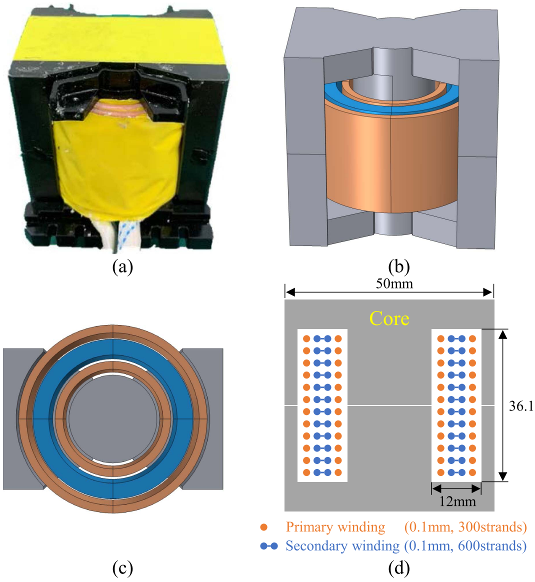

(a) (b) (c) (d)

Fig. 22. Winding structure of the designed transformer. (a) Physical map. (b) Sketch map. (c) Vertical view. (d) Section view.

Different equations can be used to calculate d_1 and d_2 according to their power ratings. PS ratio ϕ corresponding to the power intersection point can be derived as 0.25 from (18). The duty ratios d_1 and d_2 of v_p and v_s increase in the proposed methods when the transferred power rises. For different power levels, CDM and I-CDM have better performances in voltage ripple and rms current minimization than SPS. Fig. 26 shows the inductor rms current comparison with various voltage conversion ratios. Inductor rms currents can be suppressed using CDM and I-CDM schemes when M changes, and output voltage ripples have a similar tendency, as illustrated in Section IV. Therefore, the proposed CDM and I-CDM can reduce output voltage ripples and inductor rms currents effectively.

B. Output Voltage Ripple Comparison Between Calculation and Experimental Results

The output voltage harmonic component comparison between the calculation and experimental results of the 1 kW DAB converter prototype is shown in Fig. 27. There are differences between the calculation and experimental results due to the lack

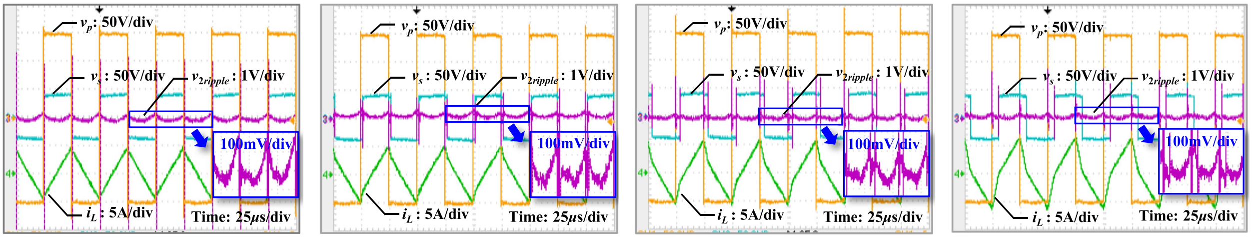

(a) (b) (c) (d)

Fig. 23. Working waveforms of the 1 kW DAB converter prototype with SPS at $M = 0.5$. (a) $P_n = 0.1$. (b) $P_n = 0.3$. (c) $P_n = 0.5$. (d) $P_n = 0.7$.

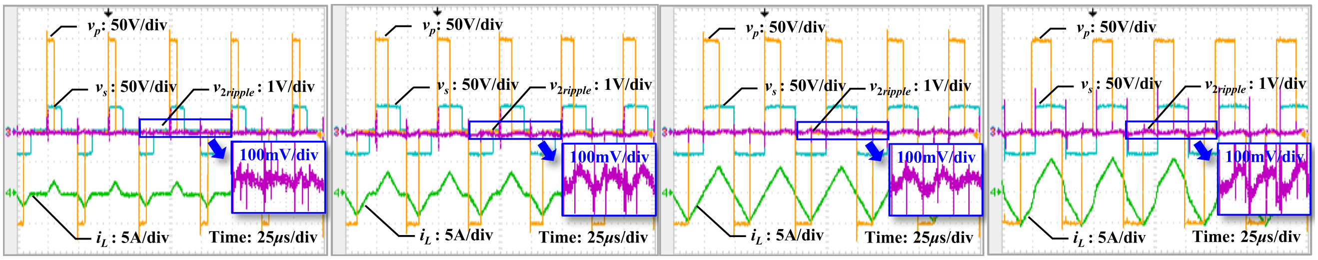

(a) (b) (c) (d)

Fig. 24. Working waveforms of the 1 kW DAB converter prototype with CDM at $M = 0.5$. (a) $P_n = 0.1$. (b) $P_n = 0.3$. (c) $P_n = 0.5$. (d) $P_n = 0.7$.

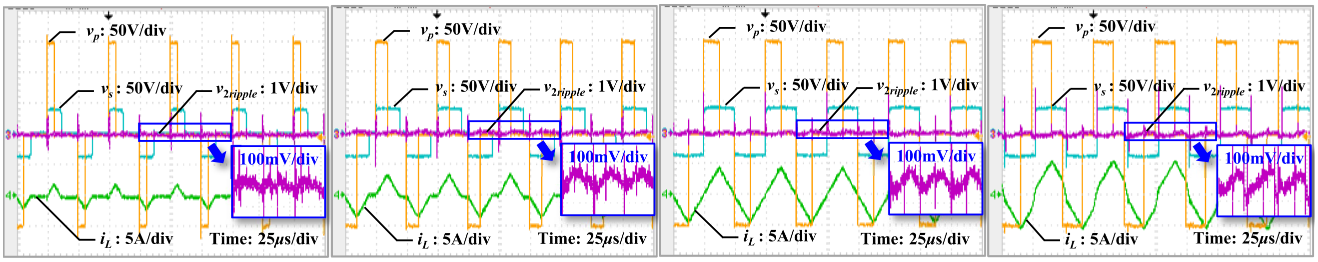

(a) (b) (c) (d)

Fig. 25. Working waveforms of the 1 kW DAB converter prototype with I-CDM at $M = 0.5$. (a) $P_n = 0.1$. (b) $P_n = 0.3$. (c) $P_n = 0.5$. (d) $P_n = 0.7$.

TABLE V
RATIO OF THE FIRST AND SECOND HARMONIC COMPONENTS OF EXPERIMENTAL RESULTS OF THE 1 KW DAB CONVERTER PROTOTYPE

Modulation schemes	Ratio of the first and second harmonic components
SPS	0.0664:1
CDM	0.0451:1
I-CDM	0.0150:1

of higher harmonics in the calculation. The theoretical value of the first harmonic component (20 kHz) of the output voltage ripple is 0. However, because of the influences of circuit parasitic parameters, deadtime, and noise interference, the actual values of the first harmonic component of SPS, CDM, and I-CDM modulation are 8.671, 2.746, and 0.910 mV, respectively. The ratio of the first and second harmonic components of experimental results is listed in Table V. The first harmonic component is far less than the second harmonic component and is usually omitted in the analysis process.

C. Output Voltage Ripples Under Different Output Capacitance and Switching Frequency

The output voltage ripple is related to the output capacitance and switching frequency. When the output capacitance is decreased for higher power density, the output voltage ripples are obvious and severe, which should be suppressed to ensure a high power quality. When the DAB converters are used in the medium- or high-voltage grid connection, the adopted switching frequency is not very high, which leads to higher output voltage ripples. Experiments are taken to explain these points.

When the output capacitance is reduced from 208.55 to 52.03 μF (the switching frequency remains 20 kHz), the waveforms of the 1 kW DAB converter prototype are shown in Fig. 28. The output voltage ripple using SPS modulation, with a value of 332.9 mV [see Fig. 28(a)], is obvious and severe. While the CDM and I-CDM are adopted to suppress the ripples, the output voltage ripples decrease to 79.7 and 76.5 mV [see Fig. 28(b) and (c)], respectively. The output voltage ripple is 85.4 mV when

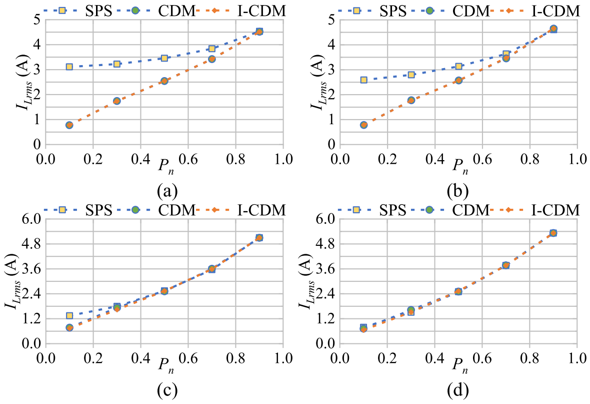

(a) (b) (c) (d)

Fig. 26. Inductor rms current of SPS, CDM, and I-CDM of the 1 kW DAB converter prototype for (a) $M = 0.4$, (b) $M = 0.5$, (c) $M = 0.75$, (d) $M = 0.875$.

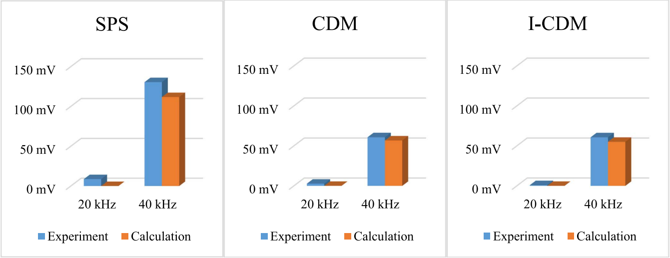

(a) (b) (c)

Fig. 27. Output voltage harmonic component comparison between calculation and experimental results of the 1 kW DAB converter prototype when $M = 0.4$ and $P_n = 0.3$. (a) SPS. (b) CDM. (c) I-CDM.

the output capacitance is 208.55 μF using SPS modulation. The effectiveness of the proposed methods has been well verified, which is equivalent to reducing the output capacitance by around 75% compared with the SPS modulation.

When the switching frequency is reduced from 20 to 10 kHz (the output capacitance remains 208.55 μF), the output voltage ripples increase, as shown in Fig. 29. The proposed methods can suppress the output voltage ripples as well.

D. *Efficiency Comparison*

The normalized efficiency curves of SPS, CDM, and I-CDM of the 1 kW DAB converter prototype before optimizing the PCB layout at $M = 0.4$, 0.5, 0.75, and 0.875 are plotted in Fig. 30, which is based on the experimental data. The SPS scheme can realize high efficiency at heavy loads. However, poor performances in efficiency can be observed due to large inductor rms currents and limited ZVS ranges when the transmission power decreases and the voltage conversion ratio deviates from 1. The efficiency of CDM and I-CDM can respectively reach 88.6% and 88.2% at $M = 0.5$ and $P_n = 0.1$, whereas the efficiency of SPS is 75.3%. CDM and I-CDM can improve the efficiency over light to medium load because of low inductor rms currents and broad ZVS ranges. While the load increases and is close to maximum, SPS, CDM, and I-CDM have similar performances. The maximum efficiency of 97.2% is achieved by I-CDM at $M = 0.875$ and $P_n = 0.3$. Therefore, CDM and I-CDM can achieve remarkable efficiency improvements. Notably, CDM has slightly higher efficiency than I-CDM at light load when M is small because more switches realize ZVS in CDM. When M approaches unity, CDM has a slightly higher rms current, which causes the efficiency deterioration of 2.1% at $M = 0.875$ and $P_n = 0.3$ than I-CDM. The specific loss analysis is as follows.

The power losses of the DAB converters are composed of three main factors: conduction losses, core losses, and switching losses [52]. The conduction losses P_{cond} stem from the ON-resistance of switches and parasitic resistances of wire. The conduction losses can be calculated as follows:

$$P_{\text{cond}} = I_{\text{Lrms}}^2(2R_{\text{on}} + 2N^2R_{\text{on}} + R_{\text{wire}}) \tag{28}$$

where N, R_{on}, and R_{wire} are the transformer turns ratio, ON-resistance of switches, and resistance of the wire, respectively.

The empirical Steinmetz equation is used to calculate the core losses P_{core} of the transformer and auxiliary inductor [53]

$$P_{\text{core}} = V_e k f_s^{\alpha} \Delta B_m^{\beta} \tag{29}$$

where k, α, and β are empirical parameters and V_e and ΔB_m are the core volume and peak induction, respectively.

The switching losses P_{sw} depend on the current and voltage of switches at the switching moment [53]. When the switches work at ZVS conditions or ZCS, P_{sw} is comparably low. Otherwise, the switches have larger switching losses.

The loss breakdown with various modulation schemes of the 1 kW DAB converter prototype is plotted in Fig. 31. It is observed that the conduction loss increases with the increase of the load and the switching loss makes up a large proportion of the total loss at light load. The core loss increases slightly when higher power is transferred. The proposed CDM and I-CDM have lower power losses over a wide power range than other modulations because of lower inductor rms current. Because the switches under the proposed methods are all working on ZVS under heavy load, the switching losses are not large compared with the conduction losses. The conduction losses account for 70.6% of the total power losses when $M = 0.5$, $P_n = 0.9$.

To increase the efficiency under light load [52], [53], the PCB routing of the gate-drive circuits can be optimized and the external gate resistor can be reduced for lower switching losses. To increase the efficiency under heavy load [52], [53], the transformer and inductor can be redesigned for lower copper losses. Thicker and short wires can be used to connect different components. The PCB routing can be optimized for lower parasitic resistances.

Therefore, the efficiency of the prototype has been improved by optimizing the PCB layout and decreasing the external gate resistance of gate-drive circuits considering the actual situation, which can reduce the conduction losses and switching losses, respectively. The original PCB of the main circuit is a two-layer PCB. The main circuit has been optimized as a four-layer PCB to reduce parasitic resistances. The PCB routing of the gate-drive circuits is also optimized to decrease the parasitic inductances for relieving the ringing of gate-drive signals. Therefore, the external gate resistor, which suppresses the ringing of gate-drive signals, can be reduced from 49.9 to 5.1 Ω, leading to lower switching losses. The experimental tests were carried out with

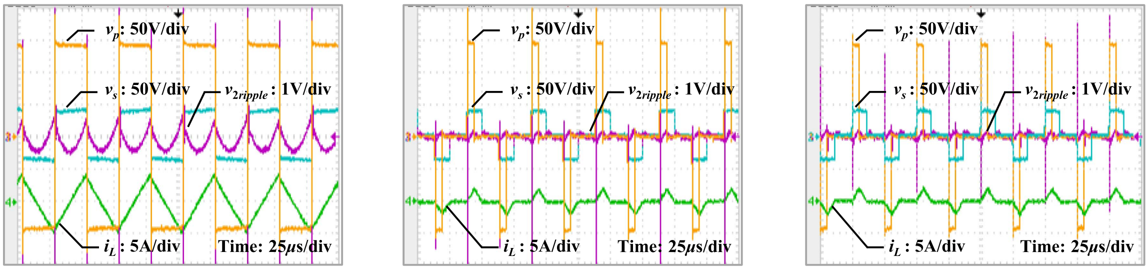

(a) (b) (c)

Fig. 28. Waveforms of the 1 kW DAB converter prototype with the output capacitance of 52.03 μF and switching frequency of 20 kHz at $M = 0.5$ and $P_n = 0.1$. (a) SPS. (b) CDM. (c) I-CDM.

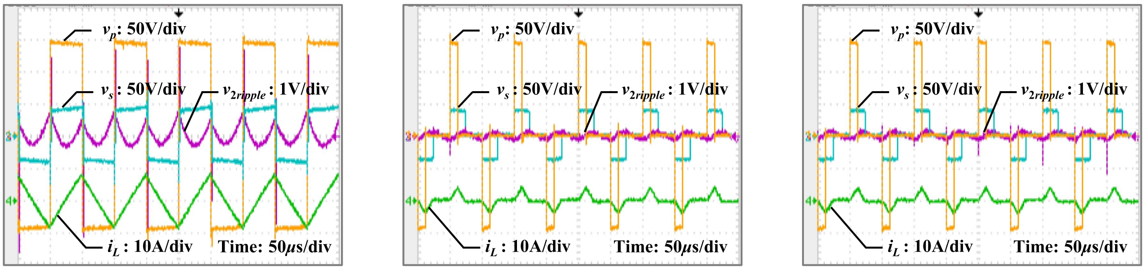

(a) (b) (c)

Fig. 29. Waveforms of the 1 kW DAB converter prototype with the output capacitance of 208.55 μF and switching frequency of 10 kHz at $M = 0.5$ and $P_n = 0.1$. (a) SPS. (b) CDM. (c) I-CDM.

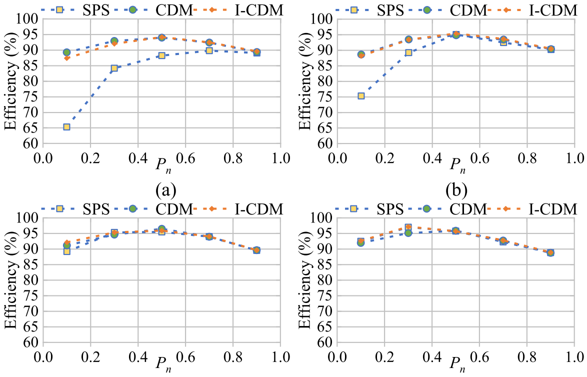

(a) (b) (c) (d)

Fig. 30. Normalized experimental efficiency curves of SPS, CDM, and I-CDM of the 1 kW DAB converter prototype before optimizing the PCB layout at (a) $M = 0.4$, (b) $M = 0.5$, (c) $M = 0.75$, (d) $M = 0.875$.

the prototype after optimizing the PCB layout. The circuit parameters of the prototype are listed in Table I. The normalized efficiency curves of the 1 kW DAB converter prototype after optimizing the PCB layout of SPS, CDM, and I-CDM at $M = 0.4$, 0.5, 0.75, and 0.875 are plotted in Fig. 32. The efficiency of the prototype after optimizing the PCB layout is improved over the whole power range compared with the one before optimization due to lower conduction losses and switching losses. I-CDM can realize the maximum efficiency of 98.4% at $M = 0.875$ and $P_n = 0.5$ after optimizing the PCB layout. It is verified that the proposed methods can achieve highly efficient transmission.

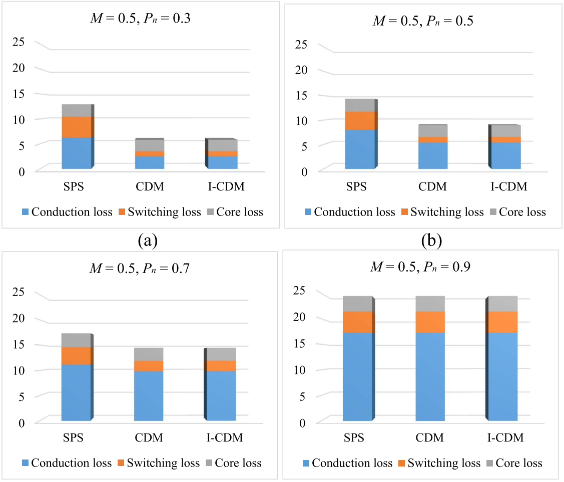

(a) (b) (c) (d)

Fig. 31. Loss breakdown with various modulation schemes of the 1 kW DAB converter prototype at $M = 0.5$ and (a) $P_n = 0.3$, (b) $P_n = 0.5$, (c) $P_n = 0.7$, (d) $P_n = 0.9$.

E. Influence of the Bandwidth on the Output Voltage Ripple

The forward path bode plot of the 1 kW DAB converter prototype under different control parameters is shown in Fig. 33. When the PI parameters $k_P = 0.005$ and $k_I = 0.1$, the crossover frequency $f_{c1} = 192$ Hz and phase margin $\varphi_{m1} = 99°$, indicating the system is stable. If the proportional parameter k_P increases to 0.01, the crossover frequency becomes 391 Hz and the bandwidth is improved.

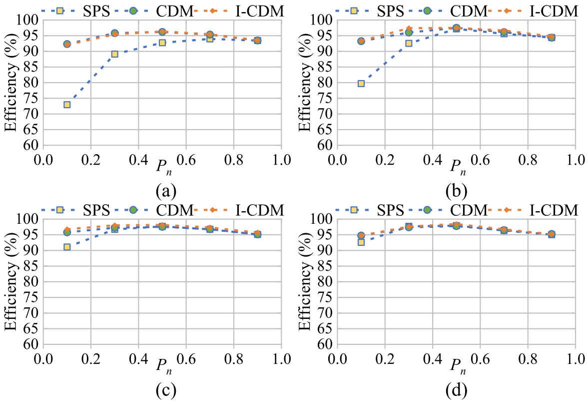

(a) (b)

(c) (d)

Fig. 32. Normalized experimental efficiency curves of SPS, CDM, and I-CDM of the 1 kW DAB converter prototype after optimizing the PCB layout at (a) $M = 0.4$, (b) $M = 0.5$, (c) $M = 0.75$, (d) $M = 0.875$.

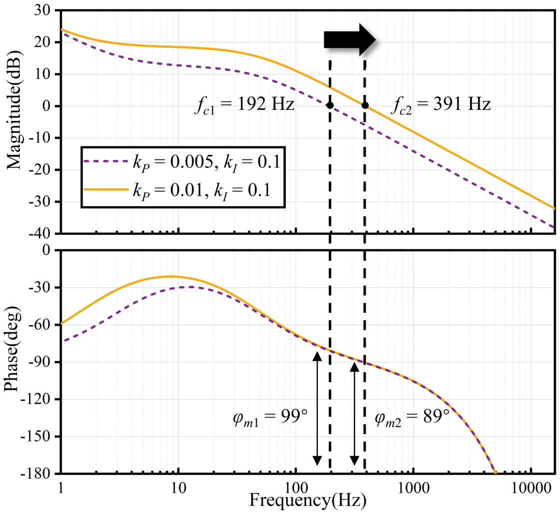

Fig. 33. Forward path bode plot of the 1 kW DAB converter prototype.

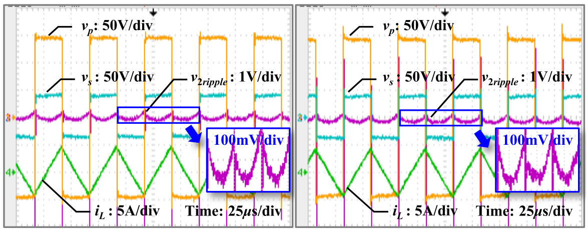

(a) (b)

Fig. 34. Experimental results of the 1 kW DAB converter prototype with SPS modulation under different control parameters when $M = 0.5$ and $P_n = 0.1$: (a) $k_P = 0.005$, $k_I = 0.1$, (b) $k_P = 0.01$, $k_I = 0.1$.

Fig. 34 shows the experimental results of the 1 kW DAB converter prototype with SPS modulation under different control parameters. The voltage ripples of $k_P = 0.005$ and $k_P = 0.01$ are 82.9 and 84.3 mV, respectively. The voltage ripple differences are very small. Because the voltage ripple is a quantity to represent the steady-state performance, the steady phase shift ratios ϕ of DAB converter systems of various bandwidths are almost the same when the load condition is not changed in

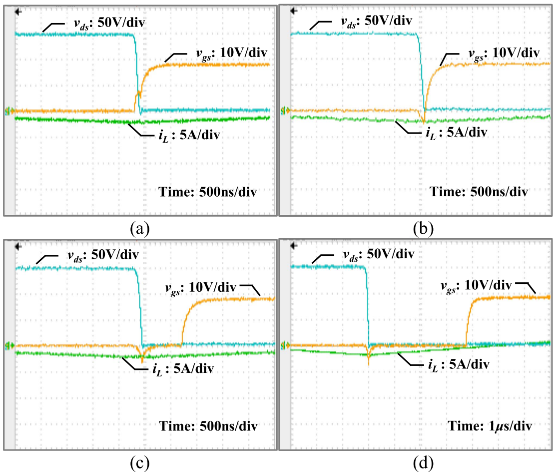

(a) (b)

(c) (d)

Fig. 35. Waveforms of S_1 with CDM modulation of the 1 kW DAB converter prototype when $P_n = 0.1$ and $M = 0.5$ under the deadtime of (a) 125 ns, (b) 250 ns, (c) 1000 ns, (c) 4000 ns.

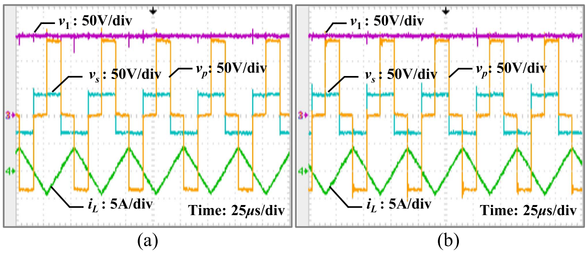

(a) (b)

Fig. 36. Waveforms of the 1 kW DAB converter prototype in the reverse power flow when $M' = 2$ and $P_n = 0.5$ with (a) CDM, (b) I-CDM.

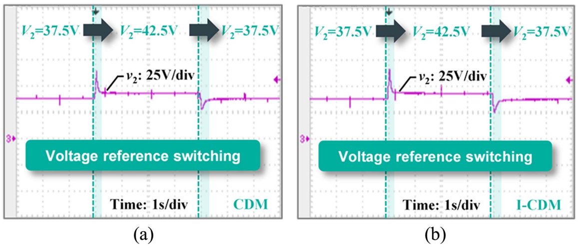

(a) (b)

Fig. 37. Dynamic waveforms of the 1 kW DAB converter prototype with voltage reference switching between 37.5 and 42.5 V at $P_n = 0.1$ using (a) CDM and (b) I-CDM.

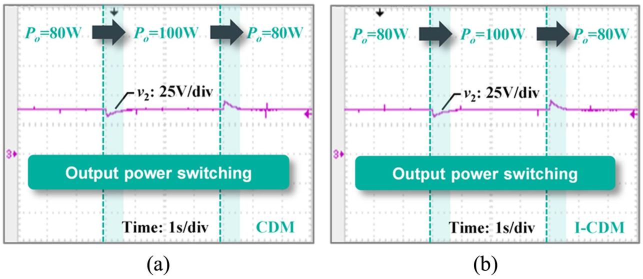

(a) (b)

Fig. 38. Dynamic waveforms of the 1 kW DAB converter prototype with load switching between 80 W and 100 W at $M = 0.5$ using (a) CDM and (b) I-CDM.

TABLE VI
PERFORMANCE COMPARISON AMONG DIFFERENT MODULATION STRATEGY

Optimized schemes	Modulation method	Analysis method	Modulation form	M range	Power range	Optimization object	Current level	Ripple characteristic	Efficiency
SPS	SPS	TDA	Online computation	Whole range	Whole range	N/A	High	N/A	Low
FDM [17]	TPS	FDA	Online computation	≤ 1	Whole range	I_{Lrms}	Medium	N/A	Medium
MRS [16]	TPS	FDA	Online computation	≥ 1	Limited range	Reactive current	Medium	N/A	Medium
GOC [26]	TPS	TDA	Online computation	Whole range	Whole range	I_{Lrms}	Low	N/A	High
DRL [19]	VF + TPS	FDA	Offline lookup table	≤ 1	Whole range	Power loss + ZVS	Low	N/A	High
OPDM [29]	ADM + PS	TDA	Online computation	≤ 1	Whole range	I_{Lpk} + ZVS	Medium	N/A	Medium
Proposed CDM	TPS	FDA	Online computation	Whole range	Whole range	$I_{Lrms} + V_{2ripple}$	Low	Considered	High
Proposed I-CDM	TPS	FDA	Online computation	Whole range	Whole range	$I_{Lrms} + V_{2ripple}$	Low	Considered	High

N/A: indicates “Not available.”

the steady state. Notably, if ϕ changes dramatically with time because of inappropriate PI parameters, the voltage ripple will vary according to the unstable ϕ.

F. Influence of the Deadtime on the ZVS

The deadtime in this work is 250 ns. To investigate the impact of deadtime on the ZVS of CDM at light load, experiments of the 1 kW DAB converter prototype with CDM modulation under different deadtime are conducted when $P_n = 0.1$ and $M = 0.5$, as shown in Fig. 35. Switches S_1, S_2, S_7, and S_8 work on ZVS under light load and their experimental results are similar. S_1 is taken as an example herein. The switch S_1 loses ZVS when the deadtime is too small from Fig. 35(a). When the deadtime of 250 ns is adopted, the ZVS of switch S_1 is achieved. If the dead time continues to increase to 1000 and 4000 ns, the ZVS is also kept. Hence, the large deadtime with CDM modulation does not induce the switch to lose ZVS under light load. However, too small or too large deadtime would cause an increase in losses and a decrease in reliability. A proper deadtime is preferred when designing the converter. The experimental test method or theoretical calculation method can be used to determine an appropriate deadtime for ZVS realization [24]. Moreover, an appropriate deadtime with CDM also ensures the ZCS of switches S_3–S_6. Similar conclusions can be drawn for I-CDM and omitted herein.

G. Case of Negative Power Flow

For negative power flow, the phase shift ratio $\phi \leq 0$, and the voltage conversion ratio $M' = V_1/(NV_2)$. The optimized modulation scheme CDM and I-CDM for reverse power flow can be acquired through a similar analysis as the positive power flow. The positive and negative power flow have similar modulation equations except for the opposite sign of ϕ and $M' = 1/M$, which is consistent with the analyses in [28]. The experiments are conducted to verify the effectiveness of CDM and I-CDM in the reverse power flow. Fig. 36 shows that the proposed modulation method can be adapted to the negative power transmission.

H. Dynamic Performance

Fig. 37 illustrates the dynamic waveforms of the 1 kW DAB converter prototype with voltage reference switching between 37.5 and 42.5 V using CDM and I-CDM. The waveforms indicate that the system can achieve a rapid response when adjusting the output voltage.

The dynamic waveforms of the 1 kW DAB converter prototype with load switching between 80 and 100 W using CDM and I-CDM are shown in Fig. 38. The system can become stable in a short time after load change by using the proposed methods. Moreover, the drop or overshoot is at an acceptable level at the switching moment. Notably, advanced control methods from recent studies can improve the dynamic performance of DAB converters [54], [55], [56]. This article is mainly devoted to improving the steady-state performance, and further improvement of dynamic performance can be studied in the near future.

I. Performance Comparison of Different Modulation Schemes

A comprehensive comparison of different modulation strategies is shown in Table VI from different aspects. In terms of modulation method, FDM [17], MRS [16], GOC [26], the proposed CDM, and I-CDM adopt TPS, whereas DRL-aided modulation [19] and OPDAM [29] use variable-frequency (VF) TPS and ADM plus PS, respectively.

From the perspective of the analysis method, TDA is utilized in SPS, GOC, and OPDM for accurate solutions. However, cumbersome mode analyses are inevitable in the TDA and other modulation schemes that adopt FDA for alleviating modeling complexity. Moreover, a multidimensional offline lookup table is needed in DRL-aided modulation to store optimization results, occupying excessive memory resources [15]. Furthermore, the proposed schemes provide expressions when $M \geq 1$ and ≤ 1 for different working conditions. As for the power range, the proposed CDM and I-CDM can be applied to the whole operation range. However, MRS has a limited power range when M is small [see Fig. 1(c)], which restricts its application. The optimized results reveal that the SPS has a higher rms current at a light load.

FDM, MRS, and OPDM can suppress rms currents. The effectiveness can also be improved [29]. The DRL-aided modulation achieves low current levels and high efficiency through extensive offline training. However, the online calculation is preferred to ensure few resources [15].

The proposed CDM and I-CDM can switch calculation expressions according to their power ranges, which guarantees their performances. The proposed CDM and I-CDM realize low inductor rms currents and high efficiency at various *M* and load conditions. Moreover, implementing the proposed modulation schemes in microprocessors is easy. Meanwhile, the proposed schemes consider the characteristics of output ripples that can be used to optimize the designs of filter capacitors and improve the power density.

In conclusion, the proposed CDM and I-CDM can reduce output voltage ripple and inductor rms currents effectively at different power ranges and voltage conversion ratios, which can improve converter efficiency and optimize circuit parameters.

VI. CONCLUSION

A CDM scheme of DAB converters has been proposed in this study to suppress output voltage ripples and inductor rms currents. The generalized averaging model considering the second harmonic component is used to represent output voltage ripples and inductor currents. The proposed CDM scheme can achieve the lowest rms current levels and output voltage ripples at light load and full power range transmission compared with SPS, FDM, and MRS. I-CDM is also proposed to realize the performance improvement of CDM at light-load and large-conversion-ratio conditions. The effectiveness of the proposed methods is validated by the 1.0 kW DAB prototype and 31.25 kW simulation platform. CDM and I-CDM can reduce around 75% output capacitance compared with the conventional SPS scheme under light load. The maximum efficiency of 98.4% is achieved by I-CDM at $M = 0.875$ and $P_n = 0.5$ after optimizing the PCB layout and decreasing the external gate resistance of gate-drive circuits. This article mainly focuses on improving the steady-state performance. The dynamic performance of the proposed methods can be improved by advanced control methods, which will be studied in the near future.

APPENDIX

A. DAB Converter Model Considering the Third Harmonic Component

The third pair of coefficients of switching functions $g_1(\tau)$ and $g_2(\tau)$ can be acquired from (4)

$$\begin{cases} \langle g_1 \rangle_3 = -2\sin(3\phi\pi)\sin(3d_1\pi/2)/(3\pi) \\ \qquad\qquad +j2\cos(3\phi\pi)\sin(3d_1\pi/2)/(3\pi) \\ \langle g_2 \rangle_3 = j2\sin(3d_2\pi/2)/(3\pi). \end{cases} \tag{30}$$

The model considering the third component of the DAB converter can be derived as follows:

$$\begin{cases} \frac{d\langle i_L\rangle_1^R}{dt} = \omega_s \langle i_L\rangle_1^I - \left(\frac{N\langle g_2\rangle_1^I}{L_S} + \frac{N\langle g_2\rangle_3^I}{L_S}\right)\langle v_2\rangle_2^I + \frac{\langle g_1\rangle_1^R\langle v_1\rangle_0}{L_S} \\ \frac{d\langle i_L\rangle_1^I}{dt} = -\omega_s \langle i_L\rangle_1^R - \frac{N\langle g_2\rangle_1^I\langle v_2\rangle_0}{L_S} + \left(\frac{N\langle g_2\rangle_1^I}{L_S} - \frac{N\langle g_2\rangle_3^I}{L_S}\right)\langle v_2\rangle_2^R \\ \qquad + \frac{\langle g_1\rangle_1^I\langle v_1\rangle_0}{L_S} \\ \frac{d\langle i_L\rangle_3^R}{dt} = 3\omega_s \langle i_L\rangle_3^I + \frac{N\langle g_2\rangle_1^I\langle v_2\rangle_2^I}{L_S} + \frac{\langle g_1\rangle_3^R\langle v_1\rangle_0}{L_S} \\ \frac{d\langle i_L\rangle_3^I}{dt} = -3\omega_s \langle i_L\rangle_3^R - \frac{N\langle g_2\rangle_3^I\langle v_2\rangle_0}{L_S} - \frac{N\langle g_2\rangle_1^I\langle v_2\rangle_2^R}{L_S} + \frac{\langle g_1\rangle_3^I\langle v_1\rangle_0}{L_S} \\ \frac{d\langle v_2\rangle_0}{dt} = \frac{2N\langle g_2\rangle_1^I\langle i_L\rangle_1^I}{C_2} + \frac{2N\langle g_2\rangle_3^I\langle i_L\rangle_3^I}{C_2} - \frac{\langle v_2\rangle_0}{R_2C_2} \\ \frac{d\langle v_2\rangle_2^R}{dt} = \left(-\frac{N\langle g_2\rangle_1^I}{C_2} + \frac{N\langle g_2\rangle_3^I}{C_2}\right)\langle i_L\rangle_1^I + \frac{N\langle g_2\rangle_1^I\langle i_L\rangle_3^I}{C_2} - \frac{\langle v_2\rangle_2^R}{R_2C_2} \\ \qquad +2\omega_s \langle v_2\rangle_2^I \\ \frac{d\langle v_2\rangle_2^I}{dt} = \left(\frac{N\langle g_2\rangle_1^I}{C_2} + \frac{N\langle g_2\rangle_3^I}{C_2}\right)\langle i_L\rangle_1^R - \frac{N\langle g_2\rangle_1^I\langle i_L\rangle_3^R}{C_2} \\ \qquad -2\omega_s \langle v_2\rangle_2^R - \frac{\langle v_2\rangle_2^I}{R_2C_2}. \end{cases} \tag{31}$$

The steady-state values **x** of i_L and v_2 can be calculated by $d\mathbf{x} = 0$, where **x** is

$$\mathbf{x} = [\langle I_L\rangle_1^R, \langle I_L\rangle_1^I, \langle I_L\rangle_3^R, \langle I_L\rangle_3^I, \langle V_2\rangle_0, \langle V_2\rangle_2^R, \langle V_2\rangle_2^I]^T. \tag{32}$$

The inductor rms current and output voltage ripple can be calculated

$$\begin{cases} I_{L\mathrm{rms}} \\ = \sqrt{(\sqrt{2}\langle I_L\rangle_1^R)^2 + (\sqrt{2}\langle I_L\rangle_1^I)^2 + (\sqrt{2}\langle I_L\rangle_3^R)^2 + (\sqrt{2}\langle I_L\rangle_3^I)^2} \\ V_{2\mathrm{ripple}} = \sqrt{(2\langle V_2\rangle_2^R)^2 + (2\langle V_2\rangle_2^I)^2}. \end{cases} \tag{33}$$

The output power considering the third harmonic component is derived in [18]

$$P_o = \sum_{k=1,3} \frac{8NV_1V_2}{k^3\pi^2\omega_s L_S}\cos\left(k\pi\frac{1-d_1}{2}\right) \times \cos\left(k\pi\frac{1-d_2}{2}\right)\sin(k\pi\phi). \tag{34}$$

B. Optimizing the Inductor Current and Output Voltage Ripple Considering the Third Harmonic Component With PSO

The optimization problem is formulated in the standard form as follows:

$$\begin{aligned} &\mathrm{Min} I_{L\mathrm{rms\_}n} and V_{2\mathrm{ripple\_}n} \\ &\text{s.t.} \begin{cases} P_{\mathrm{on}} - P_n = 0 \\ d_1 \in [0,1], d_2 \in [0,1], \phi \in [0, 0.5] \end{cases} \end{aligned} \tag{35}$$

where the per-unit value $I_{L\mathrm{rms\_}n} = I_{L\mathrm{rms}}/[NV_2/(8f_sL_s)]$, $V_{2\mathrm{ripple\_}n} = V_{2\mathrm{ripple}}/(0.01V_2)$, and $P_{\mathrm{on}} = P_o/[NV_1V_2/(8f_sL_s)]$.

A swarm of random-distributed particles in the 3-D search space is initialized first, and their velocity and position are updated as follows:

$$\begin{cases} V_i^{m+1} = \omega V_i^m + c_1 r_1 (P_{\text{best}\_i}^m - X_i^m) + c_2 r_2 (G_{\text{best}\_i}^m - X_i^m) \\ X_i^{m+1} = X_i^m + V_i^{m+1} \end{cases} \tag{36}$$

where *i* denotes the *i*th particle, *m* means the *m*th iteration, r_1 and r_2 are the random numbers between 0 and 1, c_1 and c_2 are learning factors, ω is the inertia factor, $P_{\text{best}\_i}^m$ and $G_{\text{best}\_i}^m$ are the best position particles on individual and overall swarm experience, and V_i^m X_i^m are the velocity and position of the *m*th iteration.

The fitness value can be calculated by the objective function $F(d_1, d_2, \phi)$ of the corresponding optimization problem

$$F(d_1, d_2, \phi) = I_{L\text{rms}\_n} + V_{2\text{ripple}\_n} + \mu(P_{\text{on}} - P_n)^2 \tag{37}$$

where μ is the penalty coefficient.

REFERENCES

[1] J. M. Guerrero, J. C. Vasquez, J. Matas, L. G. de Vicuna, and M. Castilla, “Hierarchical control of droop-controlled ac and dc microgrids—A general approach toward standardization,” *IEEE Trans. Ind. Electron.*, vol. 58, no. 1, pp. 158–172, Jan. 2011.

[2] T. Dragicevic, X. Lu, J. C. Vasquez, and J. M. Guerrero, “Dc microgrids—Part II: A review of power architectures, applications, and standardization issues,” *IEEE Trans. Power Electron.*, vol. 31, no. 5, pp. 3528–3549, May 2016.

[3] J. M. Guerrero, P. C. Loh, T.-L. Lee, and M. Chandorkar, “Advanced control architectures for intelligent microgrids—Part II: Power quality, energy storage, and ac/dc microgrids,” *IEEE Trans. Ind. Electron.*, vol. 60, no. 4, pp. 1263–1270, Apr. 2013.

[4] S. Inoue and H. Akagi, “A bidirectional dc-dc converter for an energy storage system with galvanic isolation,” *IEEE Trans. Power Electron.*, vol. 22, no. 6, pp. 2299–2306, Nov. 2007.

[5] H. Wu, L. Chen, and Y. Xing, “Secondary-side phase-shift-controlled dual-transformer-based asymmetrical dual-bridge converter with wide voltage gain,” *IEEE Trans. Power Electron.*, vol. 30, no. 10, pp. 5381–5392, Oct. 2015.

[6] X. Han, W. Sima, M. Yang, L. Li, T. Yuan, and Y. Si, “Transient characteristics under ground and short-circuit faults in a ±500 kV MMC-based HVdc system with hybrid dc circuit breakers,” *IEEE Trans. Power Del.*, vol. 33, no. 3, pp. 1378–1387, Jun. 2018.

[7] S. P. Engel, M. Stieneker, N. Soltau, S. Rabiee, H. Stagge, and R. W. De Doncker, “Comparison of the modular multilevel dc converter and the dual-active bridge converter for power conversion in HVdc and MVdc grids,” *IEEE Trans. Power Electron.*, vol. 30, no. 1, pp. 124–137, Jan. 2015.

[8] T. Zhao, G. Wang, S. Bhattacharya, and A. Q. Huang, “Voltage and power balance control for a cascaded H-bridge converter-based solid-state transformer,” *IEEE Trans. Power Electron.*, vol. 28, no. 4, pp. 1523–1532, Apr. 2013.

[9] J. Sun, L. Qiu, X. Liu, J. Zhang, J. Ma, and Y. Fang, “Improved model predictive control for three-phase dual-active-bridge converters with a hybrid modulation,” *IEEE Trans. Power Electron.*, vol. 37, no. 4, pp. 4050–4064, Apr. 2022.

[10] B. Zhao, Q. Song, W. Liu, and Y. Sun, “Overview of dual-active-bridge isolated bidirectional dc–dc converter for high-frequency-link power-conversion system,” *IEEE Trans. Power Electron.*, vol. 29, no. 8, pp. 4091–4106, Aug. 2014.

[11] S. Shao et al., “Modeling and advanced control of dual active bridge dc-dc converters: A review,” *IEEE Trans. Power Electron.*, vol. 37, no. 2, pp. 1524–1547, Feb. 2022.

[12] A. K. Jain and R. Ayyanar, “PWM control of dual active bridge: Comprehensive analysis and experimental verification,” *IEEE Trans. Power Electron.*, vol. 26, no. 4, pp. 1215–1227, Apr. 2011.

[13] K. S. Parihar and M. K. Pathak, “Dual mode control scheme for DAB based solid-state transformer,” *IEEE Trans. Power Electron.*, vol. 39, no. 3, pp. 3144–3155, Mar. 2024.

[14] D. Jiang et al., “Multi-objective optimization considering PET’s vibration suppression of dual active bridge converter based on BP-NSGA-II,” *IEEE Trans. Power Electron.*, vol. 39, no. 2, pp. 2226–2236, Feb. 2024.

[15] J. Yang et al., “Online digital implementation of wide voltage range rms-current-optimized control with voltage balancing capability for DAB converter,” *IEEE Trans. Power Electron.*, vol. 38, no. 4, pp. 4360–4377, Apr. 2023.

[16] T. Liu et al., “Design and implementation of high efficiency control scheme of dual active bridge based 10 kV/1 MW solid state transformer for PV application,” *IEEE Trans. Power Electron.*, vol. 34, no. 5, pp. 4223–4238, May 2019.

[17] W. Choi, K.-M. Rho, and B.-H. Cho, “Fundamental duty modulation of dual-active-bridge converter for wide-range operation,” *IEEE Trans. Power Electron.*, vol. 31, no. 6, pp. 4048–4064, Jun. 2016.

[18] B. Zhao, Q. Song, W. Liu, G. Liu, and Y. Zhao, “Universal high-frequency-link characterization and practical fundamental-optimal strategy for dual-active-bridge dc-dc converter under PWM plus phase-shift control,” *IEEE Trans. Power Electron.*, vol. 30, no. 12, pp. 6488–6494, Dec. 2015.

[19] Y. Tang et al., “Deep reinforcement learning aided variable-frequency triple phase shift control for dual active bridge converter,” *IEEE Trans. Ind. Electron.*, vol. 70, no. 10, pp. 10506–10515, Oct. 2023.

[20] Y. Tang et al., “Artificial intelligence-aided minimum reactive power control for the DAB converter based on harmonic analysis method,” *IEEE Trans. Power Electron.*, vol. 36, no. 9, pp. 9704–9710, Sep. 2021.

[21] D. Mou et al., “Optimal asymmetric duty modulation to minimize inductor peak-to-peak current for dual active bridge dc–dc converter,” *IEEE Trans. Power Electron.*, vol. 36, no. 4, pp. 4572–4584, Apr. 2021.

[22] D. Mou, Q. Luo, J. Li, Y. Wei, and P. Sun, “Five-degree-of-freedom modulation scheme for dual active bridge dc–dc converter,” *IEEE Trans. Power Electron.*, vol. 36, no. 9, pp. 10584–10601, Sep. 2021.

[23] F. Krismer and J. W. Kolar, “Closed form solution for minimum conduction loss modulation of DAB converters,” *IEEE Trans. Power Electron.*, vol. 27, no. 1, pp. 174–188, Jan. 2012.

[24] J. Li, Q. Luo, D. Mou, T. Luo, Y. Wei, and P. Sun, “Comprehensive optimization modulation scheme of low current level and wide ZVS range for dual active bridge converter with dead-zone control,” *IEEE Trans. Power Electron.*, vol. 37, no. 3, pp. 2731–2748, Mar. 2022.

[25] N. Hou, W. Song, and M. Wu, “Minimum-current-stress scheme of dual active bridge dc-dc converter with unified-phase-shift control,” *IEEE Trans. Power Electron.*, vol. 31, no. 12, pp. 8552–8561, Dec. 2016.

[26] A. Tong, L. Hang, G. Li, X. Jiang, and S. Gao, “Modeling and analysis of a dual-active-bridge-isolated bidirectional dc/dc converter to minimize rms current with whole operating range,” *IEEE Trans. Power Electron.*, vol. 33, no. 6, pp. 5302–5316, Jun. 2018.

[27] Y. Zeng et al., “Autonomous input voltage sharing control and triple phase shift modulation method for ISOP-DAB converter in dc microgrid: A multiagent deep reinforcement learning-based method,” *IEEE Trans. Power Electron.*, vol. 38, no. 3, pp. 2985–3000, Mar. 2023.

[28] M. Mahdavifard, N. Mazloum, F. Zahin, A. KhakparvarYazdi, A. Abasian, and S. A. Khajehoddin, “An asymmetrical DAB converter modulation and control systems to extend the ZVS range and improve efficiency,” *IEEE Trans. Power Electron.*, vol. 37, no. 10, pp. 12774–12792, Oct. 2022.

[29] J. Tian, F. Wang, F. Zhuo, X. Cui, and D. Yang, “An optimal primary-side duty modulation scheme with minimum peak-to-peak current stress for DAB-based EV applications,” *IEEE Trans. Ind. Electron.*, vol. 70, no. 7, pp. 6798–6808, Jul. 2023.

[30] H. Zhang, X. Tong, J. Yin, and F. Blaabjerg, “Neural network-aided 4-DF global efficiency optimal control for the DAB converter based on the comprehensive loss model,” *Energy*, vol. 262, pp. 1–12, Jan. 2023.

[31] O. M. Hebala, A. A. Aboushady, K. H. Ahmed, and I. Abdelsalam, “Generic closed-loop controller for power regulation in dual active bridge dc–dc converter with current stress minimization,” *IEEE Trans. Ind. Electron.*, vol. 66, no. 6, pp. 4468–4478, Jun. 2019.

[32] H. Shi, H. Wen, Y. Hu, and L. Jiang, “Reactive power minimization in bidirectional dc–dc converters using a unified-phasor-based particle swarm optimization,” *IEEE Trans. Power Electron.*, vol. 33, no. 12, pp. 10990–11006, Dec. 2018.

[33] H. Yang, Y. Chen, Y. Shang, C. Yu, and Y. Kang, “A temperature monitoring method for power electronic converter based on infrared image and object detection algorithm,” *IEEE Trans. Ind. Appl.*, vol. 59, no. 1, pp. 1090–1099, Jan./Feb. 2023.

[34] L. Cao, K. H. Loo, and Y. M. Lai, “Output-impedance shaping of bidirectional DAB dc–dc converter using double-proportional-integral feedback for near-ripple-free dc bus voltage regulation in renewable energy systems,” *IEEE Trans. Power Electron.*, vol. 31, no. 3, pp. 2187–2199, Mar. 2016.

[35] Z. Wang, Y. Zhang, S. You, H. Xiao, and M. Cheng, “An integrated power conversion system for electric traction and V2G operation in electric vehicles with a small film capacitor,” *IEEE Trans. Power Electron.*, vol. 35, no. 5, pp. 5066–5077, May 2020.

[36] Y. Pan et al., “Capacitance minimization and constraint of CHB power electronic transformer based on switching synchronization hybrid phase-shift modulation method of high frequency link,” *IEEE Trans. Power Electron.*, vol. 38, no. 5, pp. 6224–6242, May 2023.

[37] C. Nan, “Dual active bridge converter with PWM control in solid state transformer application,” M.S. thesis, Power Eletron. Lab., Arizona State Univ., Tempe, AZ, USA, 2012.

[38] D. Sha, X. Wang, K. Liu, and C. Chen, “A current-fed dual-active-bridge dc–dc converter using extended duty cycle control and magnetic-integrated inductors with optimized voltage mismatching control,” *IEEE Trans. Power Electron.*, vol. 34, no. 1, pp. 462–473, Jan. 2019.

[39] Z. Li, Y. Pei, L. Wang, L. Zhao, L. Pei, and W. Cao, “A comprehensive closed-loop voltage ripple control scheme for modular multilevel converter-based power electronic transformers,” *IEEE Trans. Power Electron.*, vol. 38, no. 12, pp. 15225–15241, Dec. 2023.

[40] L. Zhu, H. Bai, and A. Brown, “Model and control of a current-fed dual active bridge based ultra-wide-voltage-range auxiliary power module for 400 V/800 V electric vehicles,” *IEEE Trans. Power Electron.*, vol. 39, no. 3, pp. 3263–3276, Mar. 2024.

[41] Y. Lin, F. Zhou, G. Xu, W. Xiong, and G. Ning, “Bipolar current-fed dc-dc converter with automatic voltage balance and full range ZVS for bipolar dc system,” *IEEE Trans. Power Electron.*, to be published, doi: 10.1109/TPEL.2023.3342295.

[42] L. Xue, Z. Shen, D. Boroyevich, P. Mattavelli, and D. Diaz, “Dual active bridge-based battery charger for plug-in hybrid electric vehicle with charging current containing low frequency ripple,” *IEEE Trans. Power Eletron.*, vol. 30, no. 12, pp. 7299–7307, Dec. 2015.

[43] F. Xiong, P. Wu, H. Yang, K. Zhang, and D. Yan, “Optimization and tradeoff of dc-bus voltage ripple and DAB current stress in two-stage single-phase converter by double line-frequency power control,” *IEEE Trans. Power Eletron.*, vol. 38, no. 11, pp. 13877–13894, Nov. 2023.

[44] D. Segaran, D. G. Holmes, and B. P. McGrath, “Enhanced load step response for a bidirectional dc–dc converter,” *IEEE Trans. Power Electron.*, vol. 28, no. 1, pp. 371–379, Jan. 2013.

[45] Y.-C. Jeung and D.-C. Lee, “Voltage and current regulations of bidirectional isolated dual-active-bridge dc–dc converters based on a double-integral sliding mode control,” *IEEE Trans. Power Electron.*, vol. 34, no. 7, pp. 6937–6946, Jul. 2019.

[46] H. Bai, N. Ziling, and C. C. Mi, “Experimental comparison of traditional phase-shift, dual-phase-shift, and model-based control of isolated bidirectional dc–dc converters,” *IEEE Trans. Power Electron.*, vol. 25, no. 6, pp. 1444–1449, Jun. 2010.

[47] H. Qin and J. W. Kimball, “Generalized average modeling of dual active bridge dc–dc converter,” *IEEE Trans. Power Electron.*, vol. 27, no. 4, pp. 2078–2084, Apr. 2012.

[48] J. Huang, Y. Wang, Z. Li, and W. Lei, “Unified triple-phase-shift control to minimize current stress and achieve full soft-switching of isolated bidirectional dc–dc converter,” *IEEE Trans. Ind. Electron.*, vol. 63, no. 7, pp. 4169–4179, Jul. 2016.

[49] T. Liu et al., “High-efficiency control strategy for 10-kV/1-MW solid-state transformer in PV application,” *IEEE Trans. Power Electron.*, vol. 35, no. 11, pp. 11770–11782, Nov. 2020.

[50] D. Mou et al., “Hybrid duty modulation for dual active bridge converter to minimize rms current and extend soft-switching range using the frequency domain analysis,” *IEEE Trans. Power Electron.*, vol. 36, no. 4, pp. 4738–4751, Apr. 2021.

[51] N. Ekekwe, J. Ndubah, K. White, and O. Ben, “Practical process in high frequency distribution transformer design,” in *Proc. Elect. Insul. Conf. Elect. Manuf. Coil Winding Technol. Conf*, 2003, pp. 121–128.

[52] F. Krismer and J. W. Kolar, “Accurate power loss model derivation of a high-current dual active bridge converter for an automotive application,” *IEEE Trans. Ind. Electron.*, vol. 57, no. 3, pp. 881–891, Mar. 2010.

[53] R. Yu, G. K. Y. Ho, B. M. H. Pong, B. W.-K. Ling, and J. Lam, “Computer-aided design and optimization of high-efficiency LLC series resonant converter,” *IEEE Trans. Power Electron.*, vol. 27, no. 7, pp. 3243–3256, Jul. 2012.

[54] Y. Zeng et al., “Deep reinforcement learning-enabled distributed uniform control for a dc solid state transformer in dc microgrid,” *IEEE Trans. Ind. Electron.*, vol. 71, no. 6, pp. 5818–5829, Jun. 2024.

[55] J. Sun, L. Qiu, X. Liu, J. Ma, and Y. Fang, “Model-free moving-discretized-control-set predictive control for three-phase dual-active-bridge converters,” *IEEE Trans. Power Electron.*, to be published, doi: 10.1109/TPEL.2023.3309137.

[56] Z. Bu, W. Zhao, M. Zhang, J. Teng, X. Li, and X. Sun, “Dynamic performance evaluation and optimization of common HFac bus lightweight MMC-SST,” *IEEE Trans. Power Electron.*, vol. 39, no. 2, pp. 2035–2050, Feb. 2024.

Xiaofeng Wang (Student Member, IEEE) was born in Anhui, China, in 1997. He received the B.S. degree in electrical engineering from Southwest Jiaotong University, Chengdu, China, in 2019. He is currently working toward the Ph.D. degree in electrical engineering in the State Key Laboratory of Power Transmission Equipment and System Security and New Technology, Chongqing University, Chongqing, China.

His major research interests include flexible dc transmission and solid-state transformers.

Ming Yang (Senior Member, IEEE) received the B.S. and Ph.D. degrees in electrical engineering from Chongqing University, Chongqing, China, in 2009 and 2014, respectively.

He was a Postdoctoral Fellow with the New York University Tandon School of Engineering, Brooklyn, NY, USA, from 2016 to 2018. He is currently a Professor with the State Key Laboratory of Power Transmission Equipment and System Security and New Technology, Chongqing University. His research interests include electromagnetic transient simulation and transformer modeling, overvoltage in power systems, flexible dc transmission, and solid-state transformers.

Wenxia Sima (Member, IEEE) was born in Henan, China, in 1965. She received the B.S. and Ph.D. degrees in electrical engineering from Chongqing University, Chongqing, China, in 1988 and 1994, respectively.

She is a Professor with the State Key Laboratory of Power Transmission Equipment and System Security and New Technology, Chongqing University. Her research interests include flexible dc transmission, electromagnetic transient simulation, and transformer modeling.

Tao Yuan (Member, IEEE) received the B.S. degree in electrical engineering from Sichuan Polytechnic Institute, Sichuan, China, in 1999, and the M.S. and Ph.D. degrees in electrical engineering from Chongqing University, Chongqing, China, in 2001 and 2010, respectively.

He is currently an Associate Professor with Chongqing University. His research interests include overvoltage protection and grounding technology in power systems.

Potao Sun (Member, IEEE) was born in Henan, China, in 1989. He received the Ph.D. degree in electrical engineering from Chongqing University, Chongqing, China, in 2016.

He worked on lightning protection as a joint training Doctoral in electrical engineering with the University of Florida, USA, in 2014. He is currently an Associate Professor with the State Key Laboratory of Power Transmission Equipment and System Security and New Technology, Chongqing University. His major research interests include overvoltage protection of power transformers.

Shuoyan Lin was born in Hunan, China, in 2001. He received the B.S. degree in electrical engineering from China University of Mining and Technology, Xuzhou, China, in 2022. He is currently working toward the M.S. degree in electrical engineering in the State Key Laboratory of Power Transmission Equipment and System Security and New Technology, Chongqing University.

His major research interests include solid-state transformers and harmonic state estimation of power system.